Spring 2012

Emission from O_2 Gas in the Kleinman-Low Region of the Great Nebula in Orion

Michael Denney Turner
San Jose State University

EMISSION FROM O_2 GAS IN THE KLEINMAN-LOW REGION OF THE GREAT NEBULA IN ORION

A Thesis

Presented to

The Faculty of the Department of Physics and Astronomy

San José State University

In Partial Fulfillment

of the Requirements for the Degree

Master of Science

by

Michael D. Turner

May 2012

The Designated Thesis Committee Approves the Thesis Titled

EMISSION FROM O_2 GAS IN THE KLEINMAN-LOW REGION OF THE GREAT NEBULA IN ORION

by

Michael D. Turner

APPROVED FOR THE DEPARTMENT OF PHYSICS AND ASTRONOMY

SAN JOSÉ STATE UNIVERSITY

May 2012

Dr. Michael Kaufman	Department of Physics and Astronomy
Dr. Monika Kress	Department of Physics and Astronomy
Dr. Patrick Hamill	Department of Physics and Astronomy

ABSTRACT

EMISSION FROM O_2 GAS IN THE KLEINMAN-LOW REGION OF THE GREAT NEBULA IN ORION

by Michael D. Turner

We calculated line intensities of ground-state emission from atomic ([O I]) and molecular (O_2) oxygen under various conditions of temperature (10–10^4 K) and density (10–10^4 cm^{-3}) in photodissociation regions (PDR) of molecular gas clouds, with UV flux intensity (G_0) of 10^5. Using a magnetohydrodynamic shock model to produce profile data in a range of pre-shock velocities ($5 \leq v_s \leq 20$ km s^{-1}) and a range of pre-shock H and H_2 gas densities (10^3–10^5 cm^{-3}), we calculated line intensities for both [O I] and O_2 emission. Finally, we used these tools successfully to find a model that best describes the recent observations made by the Herschel Oxygen Project team of the 487 GHz, 774GHz, and 1121 GHz lines of O_2 in the Kleinman-Low region of the Great Nebula in Orion. Assuming that the source fills all the beams, our calculated 1121/774 intensity ratio falls well outside the statistical uncertainty limits of the observed ratio. Alternatively, assuming that the source fills the 1121 GHz beam, but not the 774 GHz and 487 GHz beams, we found source diameters which produce ratios equal to the mean values for the observed beam ratios.

DEDICATION

- To the "pleasure of finding the thing out."—Richard P. Feynman
- To the memory of George O. Abell, an extraordinary teacher and true Renaissance man, who, in one short summer, opened my eyes to the cosmos, and my ears to Richard Wagner.

ACKNOWLEDGEMENTS

I wish to thank all those who have contributed to my successful completion of this paper and the underlying research; in particular, to Dr. Michael Kaufman, my advisor, for patiently guiding me through heretofore (for me) unexplored areas of astrophysics, including the arcana of astronomical spectroscopy; and, for re-introducing me to what was thought to be an extinct language—Fortran. I especially thank my wife, who has patiently supported me through the rough spots in this process.

TABLE OF CONTENTS

CHAPTER

LIST OF TABLES

Table

LIST OF FIGURES

Figure

CHAPTER 1

INTRODUCTION

1.1 Molecular clouds and star formation

The space between star systems in galaxies is filled with a thin mix of hydrogen, helium, oxygen, and other species in molecular, atomic, and ionized (gas) form as well as dust (solid state) and electrons. Number densities of the gas can range from $\sim .5$ cm^{-3} in warm neutral gas not confined to clouds, to 10^4 cm^{-3} in hot diffuse regions, to 10^6 cm^{-3} in cold dense molecular clouds. By comparison, the density of air on the earth's surface is roughly 2×10^{19} cm^{-3}. Most of the matter is gaseous (about 99%, by mass), with dust constituting most of the remaining 1% (Tielens [Tie05]).

There are three phases in thermal pressure equilibrium: cold molecular clouds, warm inter-cloud gas, and hot coronal gas. The main sources of heating are stellar photons, high-energy protons, and X-rays. Cooling takes place through fine-structure atomic emission that dominates in most regions,[1] except in hot gas and deep inside molecular clouds, where cooling takes place through collisional excitation, then de-excitation through fine-structure emissions. Fine-structure emission in the ground level of C II and O I dominate in the cold neutral medium,[2] while other ionized species dominate in the much hotter H II regions. In higher temperature regions, collisional excitation of the $n = 2$ and $n = 3$ levels of hydrogen

[1] Fine-structure emission refers to closely spaced emission lines resulting from spin-orbital coupling.

[2] II refers to singly ionized atoms, I to neutral atoms and the brackets (when used) indicate "forbidden" transitions.

produce electronic transitions that are the source of cooling emission, while rotational transitions of molecular species are important cooling mechanisms for cool molecular clouds (Tielens [Tie05]).

Stars are born, evolve, and die in the interstellar medium (ISM). While dust and gas clouds undergo gravitational collapse to form stars, these same stars eject dust and gas, photons, and protons into the ISM. This cyclic process has driven the origin and evolution of galaxies, including our own Milky Way. High mass stars, through winds and supernovae, support clouds against both galactic and self-gravity. The radiative cooling mechanism by molecules in the cold molecular region leads to gravitational instability and collapse to form stars. The massive stars also supply the energy sources—far ultraviolet photons and cosmic ray protons—that are the main heating, dissociation, and ionization sources for the gas. The elements that make up dust are supplied through coronal mass ejection and supernova explosions (Tielens [Tie05]).

These processes constitute a vast feedback control system that regulates the physical and chemical evolutionary processes in every star and galaxy, from the very earliest stars and galaxies to the present. We can understand these processes only through observation of the radiative output from these gas clouds and by developing physical and chemical models that accurately predict these observations. Our interest here will be specifically directed toward photodissociation regions, cold molecular clouds, and continuous shock conditions in those molecular clouds.

In order to understand the processes involved in the complex interaction between the stars and the medium in which they are born, evolve, and to which their ashes are returned, we must be able to measure such physical parameters as density, temperature, and abundances of atomic and molecular species, magnetic fields, gas velocities, and more. These measurements cannot be made directly;

instead, we must use whatever information can be extracted from radiative emissions from the cloud zones. To quantify these processes, mathematical models must be constructed that predict intensities and types of emissions from certain species under various physical conditions. Thus, physical conditions and processes can be inferred from actual observations of the intensities of these emissions.

1.2 Atomic and molecular oxygen in molecular clouds

For example, the ratio of intensities of the [C II] 158 μm and [O I] 63 μm lines will give a constraint on temperature and density, while the ratio of intensities of the [O I] 63 μm and 145 μm lines give a constraint on H density. The [O I] 145 μm line intensity gives the column density of atomic oxygen if temperature and density are known, while the [O I] 63 μm line intensity gives a measure of temperature. The measurements of all three lines together can give uniquely the temperature, density of H, and abundance of O I in the PDR being observed (Tielens [TH85]).

In spite of the importance of O_2 in the production of larger molecular species that have been detected in recent years, O_2 in the ISM has only very recently been detected. One reason for O_2's elusiveness has been that Earth's O_2-rich atmosphere makes direct observation of O_2 emission impossible from ground-based telescopes. Only space telescopes are able to detect these emissions ([GMB$^+$00]).

In subsequent chapters, we will discuss:

- the physical conditions and chemical makeup of photodissociation and shock regions (chapter 2).
- the spectroscopy of ground-state fine-structure emissions from O I and O_2 (chapter 3).
- the C-shock model and line intensity calculations (chapter 4).

- observations of O_2, the Herschel Oxygen Project; applying the model to reproduce those observations (chapter 5).
- our summary of findings and conclusions (chapter 6).

CHAPTER 2

CLOUD REGIONS: PHYSICAL CONDITIONS AND CHEMICAL MAKEUP

2.1 Photodissociation regions

Figure 2.1 depicts a photodissociation region (PDR) illuminated by far UV radiation from a nearby O or B star, or a group of such stars. Depth into the PDR is represented by A_v, the dust extinction in magnitudes at visual wavelengths. The gas near the cloud surface is heated to temperatures in the range of 100 to 1000 K. The gas is mainly atomic except for species with ionization potentials below the Lyman limit, such as C^+, S^+, Si^+, and Fe^+. Deeper into the cloud ($A_v \sim 1.2$) we find atomic C and CO. At $A_v \sim 3$–8 will be found atomic O , then O_2, H_2O and OH, which are characteristic of a cold molecular cloud where photodissociation is no longer important. Cooling in the PDR is dominated by the [C II] 158 μm and [O I] 63 μm lines, while cooling in the cold molecular cloud is dominated by the molecular rotational lines of O_2, H_2O and OH.

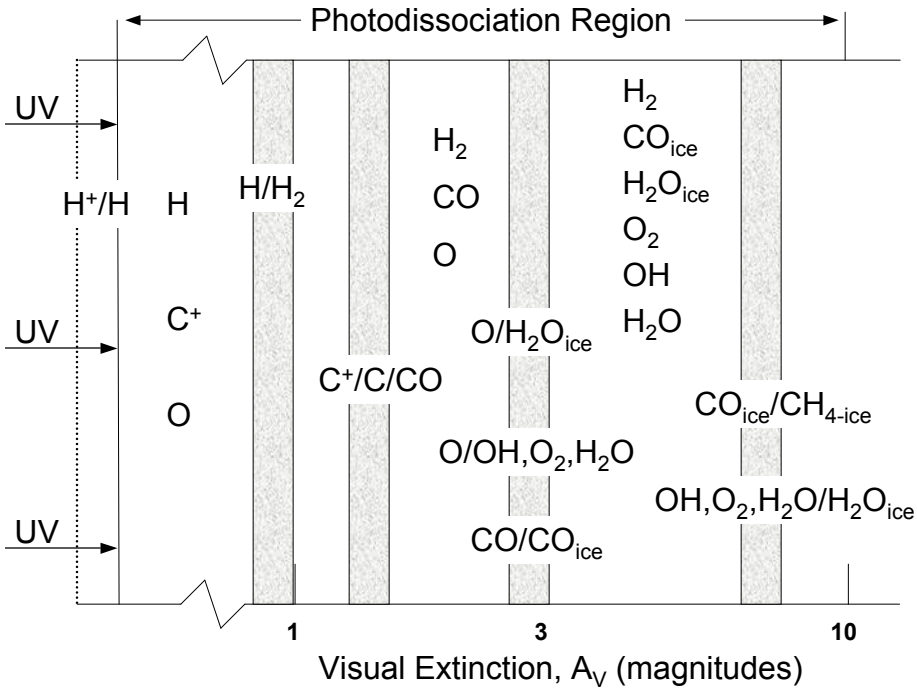

Figure 2.1: Layered structure of a photodissociation region. Intense far-UV radiation from hot (O,B) stars is incident from the left.

From Figure 2.1, we see that as the UV flux is attenuated, ionized hydrogen (H^+) transitions to fully neutral hydrogen (H). Photons with energies less than 13.6 eV will dissociate molecular hydrogen (H_2) and ionize carbon, forming an H/C^+ region. Around $A_v \sim 1$, H_2 dominates, since the UV flux is attenuated enough to dissociate only a small fraction of the H_2 molecules. Going deeper into the cloud ($A_v \sim 1.5$) the flux has attenuated to the point that the ionized carbon (C^+) recombines to form neutral C and combines with OH to form CO molecules. Around $A_v \sim 3$–6, the flux is insufficient to ionize oxygen atoms or molecules, which then become the dominant forms of oxygen.

In the C^+/C/CO transition, C forms CO through two reactions:

$$C + OH \rightarrow CO + H \text{ and } C + O_2 \rightarrow CO + O$$

while O_2 results from:

$$O + OH \rightarrow O_2 + H \ .$$

The abundances of the oxygen-bearing molecules OH, O_2 and H_2O, increase with greater depth in the cloud since photodissociation becomes much less important.

2.2 Shock zones

A shock wave is a discontinuity in the medium resulting from supersonic material traveling faster than the local speed of sound; that is, faster than information can travel in the medium. The slow-moving medium cannot respond to the fast material before it arrives. In fast shocks (J-shocks), the moving gas is stopped so suddenly and heated to such high temperatures that little radiative and non-radiative relaxation can take place. Weak continuous shocks (C-shocks) occur in dense, molecular gas with a low degree of ionization, a moderate (or larger) magnetic field, and relatively low shock velocities. The shock front is much thicker than the cooling length scale.

Figure 2.2(a) shows a typical velocity profile for a C-shock with pre-shock velocity, $v_s = 12$ km s^{-1} and pre-shock H_2 density of 2×10^4 cm^{-3}. The shock is "cushioned" by the presence of a strong magnetic field, limiting the temperature rise due to compression, thereby limiting dissociation of H_2 that allows cooling via atomic fine-structure and molecular rotational transitions, further limiting the temperature, and thus preserving the molecular species. The temperature through the shock zone may go high enough ($\sim$ 500 K), however, to force some of the O and

O_2 into H_2O (See Figure 2.2(b):

$$O + H_2 \rightarrow OH + H, \text{ and } OH + H_2 \rightarrow H_2O + H.$$

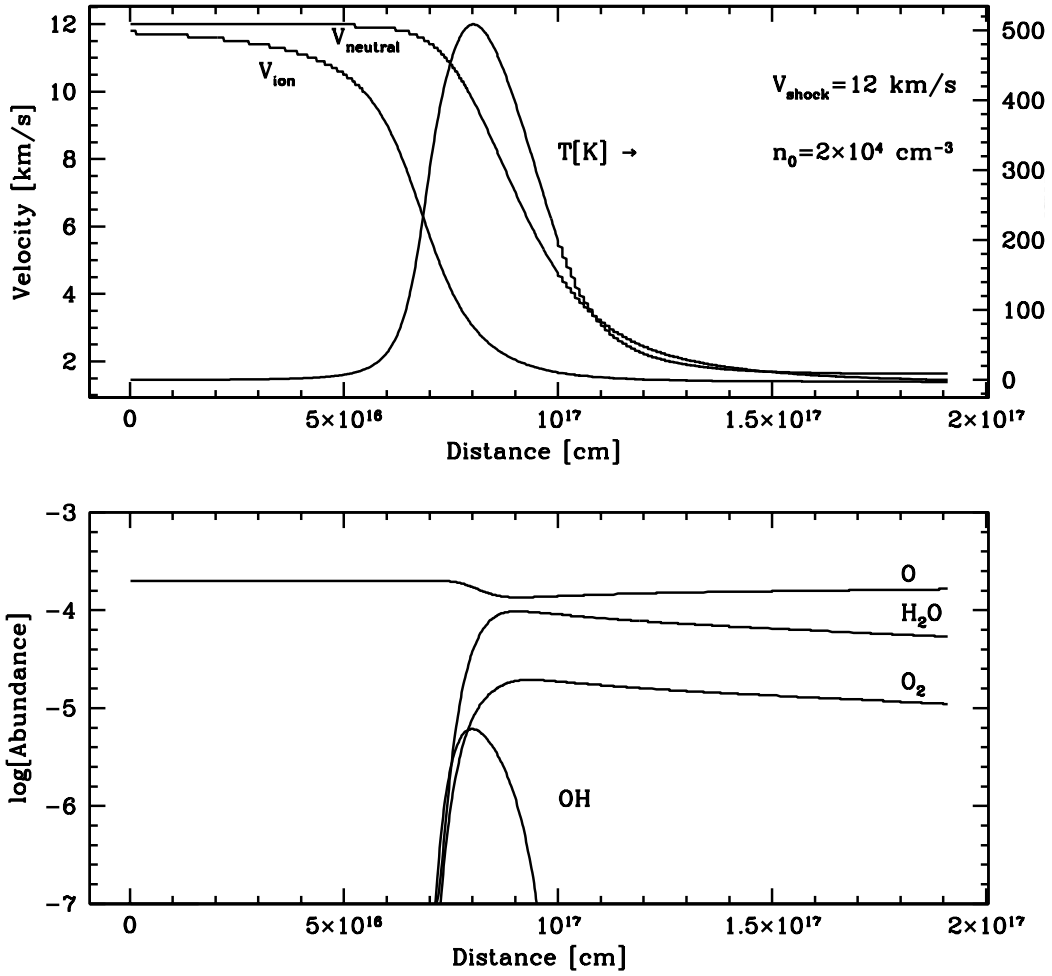

Figure 2.2: (a) Typical shock velocity profile, v_s = 12 km s^{-1}, n = 2×10^4 cm^{-3}, (b) Species abundance through the shock zone. Provided courtesy of M. J. Kaufman (private communication).

CHAPTER 3

O I AND O_2: SPECTROSCOPY AND FINE-STRUCTURE EMISSION

3.1 General concepts and definitions

Due to the quantization of energy levels, atoms absorb and emit electromagnetic radiation ("photons") at characteristic wavelengths. Spectral "lines" at a given wavelength are produced when the atom transitions from a given energy level to a lower energy level. The wavelength, λ, and related frequency, ν, are given by

$$E = hc/\lambda = h\nu \tag{3.1}$$

We will, henceforth, refer to spectral lines only in terms of frequency.

Not only do these spectral lines serve as a unique identifier for a particular atomic species, they also provide other useful information about the physical environment in which that species resides. While free electrons may absorb and emit photons at any frequency,[1] bound electrons will only transition to a higher level when the photon energy is equal to the energy difference between the levels, as given by equation 3.1. Atoms in an excited state (a state of higher energy than the ground state, or lowest possible energy level) may spontaneously drop to a lower energy state by emitting photons at the frequency associated with the energy difference between levels. Note that only atoms in an excited state (above the ground state) can emit photons.

The probability of photon emission from an excited atom with frequency ν_{ji} is A_{ji}, and is called the Einstein A coefficient for spontaneous emission. It gives the

[1] For example, Bremsstrahlung, or free-free radiation

number of transitions per second of atoms from energy state j to a lower state i. Similarly, there is a corresponding Einstein B coefficient which is the probability with which an atom will absorb a photon with frequency ν_{ji} and transition from lower state i to higher state j. These coefficients can be calculated for any given transition of any atomic or molecular species and are tabulated in various databases.

Atoms can also undergo transitions by way of stimulated emission of photons of the same frequency as the transition energy of the atoms. The emitted photons and the incident photons have the same frequency and phase (i.e., they are coherent). If there is a large population of atoms in the excited state, an avalanche of coherent photons can take place. This is known as laser action—a familiar phenomenon in the laboratory as well as in commercial products. The mechanism for this to take place is population inversion—a condition where the excited levels have a greater population than the lower levels. When the frequencies involved are at lower frequencies, such as microwaves and far-infrared, the phenomenon is called "masing" behavior. We will discuss this later in the context of shocked oxygen atoms.

To the extent that atomic or molecular species absorb the spectral lines of the same species in a line-of-sight observation through a molecular cloud, we may consider those spectral lines to be "optically thick" or "optically thin". The measure of this is τ, the optical depth, which is defined by

$$\tau = \int K dz \tag{3.2}$$

where K is the product of the number density of the species and an absorption coefficient; z is the cloud depth. In the cases to be considered here, spectral lines are optically thin; consequently, the observed intensity is directly proportional to the column density, allowing us to easily compute the column density from the

observed intensity.

Besides the radiative processes described above, collisions with other species can excite or de-excite atoms (and molecules). In the case of molecular clouds, the dominant collision partners are atomic and molecular hydrogen. The transition rates are proportional to the number density of the collision partners and the collision excitation and de-excitation rate coefficients c_{ij} and c_{ji}. The de-excitation rates are determined through laboratory experiments and quantum mechanical calculations, while the excitation rates are calculated from the de-excitation rates as follows:

$$c_{ij} = c_{ji}\frac{g_j}{g_i}e^{-(E_j-E_i)/kT} \tag{3.3}$$

The criterion for determining whether a particular emitting species behaves as if it is in local thermodynamic equilibrium (LTE) is the critical density, n_{cr}, the density at which the radiative lifetime (A_{ji}^{-1}) is approximately equal to the mean time between collisions, i. e.,

$$n_{cr} = \frac{\sum_{i<j} A_{ji}}{\sum_{i\neq j} c_{ji}} \tag{3.4}$$

We will use this later to verify whether our LTE assumptions are appropriate.

3.2 Spectroscopy

3.2.1 Energy levels and quantum numbers

Atomic states are characterized by their quantum numbers: the principal quantum number, n; the orbital angular momentum quantum number, l; and the spin angular momentum quantum number, s.

The principal quantum number, n, arises from the radial solutions of the Schrödinger wave equation for the hydrogen (or hydrogen-like) atom, with eigenvalues

$$E_n = -R\frac{Z^2}{n^2} \tag{3.5}$$

where Z is the atomic number and n is the principal quantum number. R is the Rydberg constant = 109737.31 cm^{-1} (13.6 eV). So, for a transition from the ground state ($n = 1$) to the first excited state ($n = 2$), the transition energy (ΔE) would be $\frac{3}{4}R$, or 82258.2 cm^{-1} (10.2 eV). This energy corresponds to a temperature of 118361 K—more like a stellar interior than a cool gas cloud. In the region we are exploring, it is very clear that we will be dealing only with atoms and molecules in the ground state.

The orbital angular momentum quantum number, l, (and m, the magnetic quantum number, important in magnetic field interactions) arises from the azimuthal solutions of the Schrödinger wave equation; l can take values of $0, 1, \cdots n-1$, while m can take on values of $-l, -l+1, \cdots, l-1, l$. Note that for atoms more complex than hydrogen and helium, electrons occupy levels $n > 1$ in the ground state.

The fourth quantum number, s, is the projection of spin angular momentum (that is, $s = \pm\frac{1}{2}$ per electron) in the z-axis of the system. Quantum number s can take on values of $-s, -s+1, \cdots, s-1, s$.

Since we are concerned here only with fine-structure transitions within a given energy level, we will not be concerned with the principal quantum number, n. So the energy levels of an atom are characterized by the magnitude of the total angular momentum—the vector sum of the orbital and spin angular momenta:

$$J = |\boldsymbol{J}| = |\boldsymbol{L} + \boldsymbol{S}| \tag{3.6}$$

where $\boldsymbol{L}$ and $\boldsymbol{S}$ are the vector sums of the orbital angular momenta and spin angular momenta of each electron, with each electron having a spin of $+\frac{1}{2}$ or $-\frac{1}{2}$. Total J can take $2S+1$ possible values: $L+S, L+S-1, \cdots, |L-S|+1, |L-S|$. Electron spin produces a spin magnetic moment; orbital motion produces an orbital

magnetic moment. The resulting spin-orbit coupling splits each J level into sublevels, separated by $\sim 10^{-1}$–10^{-2} eV. (See Figure 3.1, for example.) This phenomenon, known as "fine-structure splitting", generally results in emission in the near- to far-infrared spectrum (Tennyson [Ten05],Tielens [Tie05]).

3.2.2 Spectroscopic notation

Orbital momenta are designated by s,p,d,f, ..., which refer to the orbital quantum numbers $l = 0, 1, 2, 3, \ldots$. For example, the electronic configuration of the oxygen atom would be written: $1s^2 2s^2 2p^4$, meaning that oxygen has two electrons at the $n = 1, l = 0$ level (filling that level), 2 electrons in the $n = 2, l = 0$ subshell (filling it), and 4 electrons at the $n = 2, l = 1$ subshell.

The energy levels are designated by spectroscopic hieroglyphs, called "term symbols", using the general format, ${}^{2S+1}L_J$ (sometimes including a superscript o to indicate odd parity). L is the value $L = 0, 1, \ldots$, represented by the capital letters $S, P, D, \ldots$, corresponding to the L values. S is total spin, and J is total angular momentum. So, for example, the $S = 1$, $J = 2$, $L = 1$ state of the oxygen atom would be represented by the term symbol ${}^3P_2$. We will not discuss selection rules in detail, but in the case of magnetic dipole transitions with spin-orbital coupling, $\Delta S = 0, \Delta L = 0$, and $\Delta J = \pm 1$ For the ${}^3P$ ground state of oxygen, the only three possible terms, in decreasing order of energy, are ${}^3P_0$, ${}^3P_1$, and ${}^3P_2$. Figure 3.1, below, shows an energy level diagram of the ${}^3P$ ground state levels, and allowed transitions.

Molecules are more complex, but diatomic molecules can be described in ways analogous to single atoms. For homonuclear diatomic molecules, such as O_2, levels are characterized by the component of total angular momentum along the axis between the two nuclei, and can take values m_l between $l, l-1, \ldots, -l$. Then

$\lambda = |m_l| = 0, 1, \cdots$ which, by convention, are assigned the Greek letters $\sigma, \pi, \delta, \cdots$, just as the letters s,p,d,... are assigned to the atomic orbitals. The general form of the term symbol for homonuclear diatomic molecules is ${}^{2S+1}\Lambda^{\pm}_{u,g}$ where Λ is the sum of the λ's; for $\Lambda = 0, 1, 2, \ldots$, we use the symbols $\Sigma, \Pi, \Delta, \ldots$. The subscript g or u indicates whether switching the position of the two nuclei changes the sign of the wave function. If there is no change of sign, the state is symmetric or "gerade" or "g". If the state is antisymmetric, it is "ungerade", or "u". The superscript, which may be + or -, is another symmetry indicator that applies only to the Σ states. It is almost always + (in which case it is omitted), except for the O_2 molecule whose ground state configuration gives the lowest state of symmetry, ${}^3\Sigma_g^-$ (Tennyson [Ten05]). The term symbol for the ground state of O_2 is $X^3\Sigma_g^-$. The X emphasizes that this is the electronic ground state. Common notation for describing these energy levels is (N, J) or, N_J; transitions are shown as $N_{Ji} - N_{Jj}$. So, for example, the 487 GHz line of O_2 would be represented by $3_3 - 1_2$.

3.3 [O I] in photodissociation regions and C-shocks

At the low temperatures encountered in these regions, we are concerned only with the fine-structure forbidden transitions of O I in the ${}_3$P ground state. The important transitions are: ${}^3P_0 \rightarrow {}^3P_1$ (145 μm) and ${}^3P_1 \rightarrow {}^3P_2$ (63 μm), both magnetic dipole transitions. Figure 3.1 illustrates the splitting of the ^{3}P ground state.

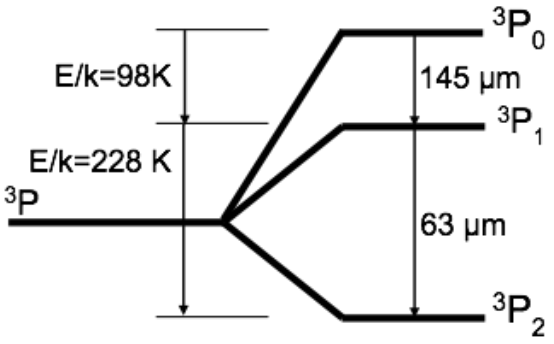

Figure 3.1: Fine-structure transitions of the ^{3}P ground state of O I

3.4 O_2 in C-shocks

O_2 has no electric dipole moment, but, thanks to having two unpaired electrons, it does have a magnetic dipole moment which gives rise to the $X^3\Sigma_g^-$ fine structure; the rotational levels are split by spin-rotation coupling. S, the total spin angular momentum number, is 1. N, the total angular momentum number takes only odd values, $N = 1, 3, 5 \ldots$, since the nuclei are identical spin 0 bosons. The total angular momentum quantum number for the molecule, $J = N + S$, can take values of $N-1$, N, or $N+1$; consequently, each rotational level is split into a triplet.

We are concerned here with the transitions between these lines in particular: the 487 MHz ($3_3 - 1_2$), the 774 MHz ($5_4 - 3_4$), and the 1121 MHz ($7_6 - 5_6$) lines. These lines have very low spontaneous emission rates ($\sim 10^{-8}$ s^{-1}), and so are optically thin in the molecular cloud environment of concern. Figure 3.2 shows the rotational levels of the $X^3\Sigma_g^-$ ground state of O_2.

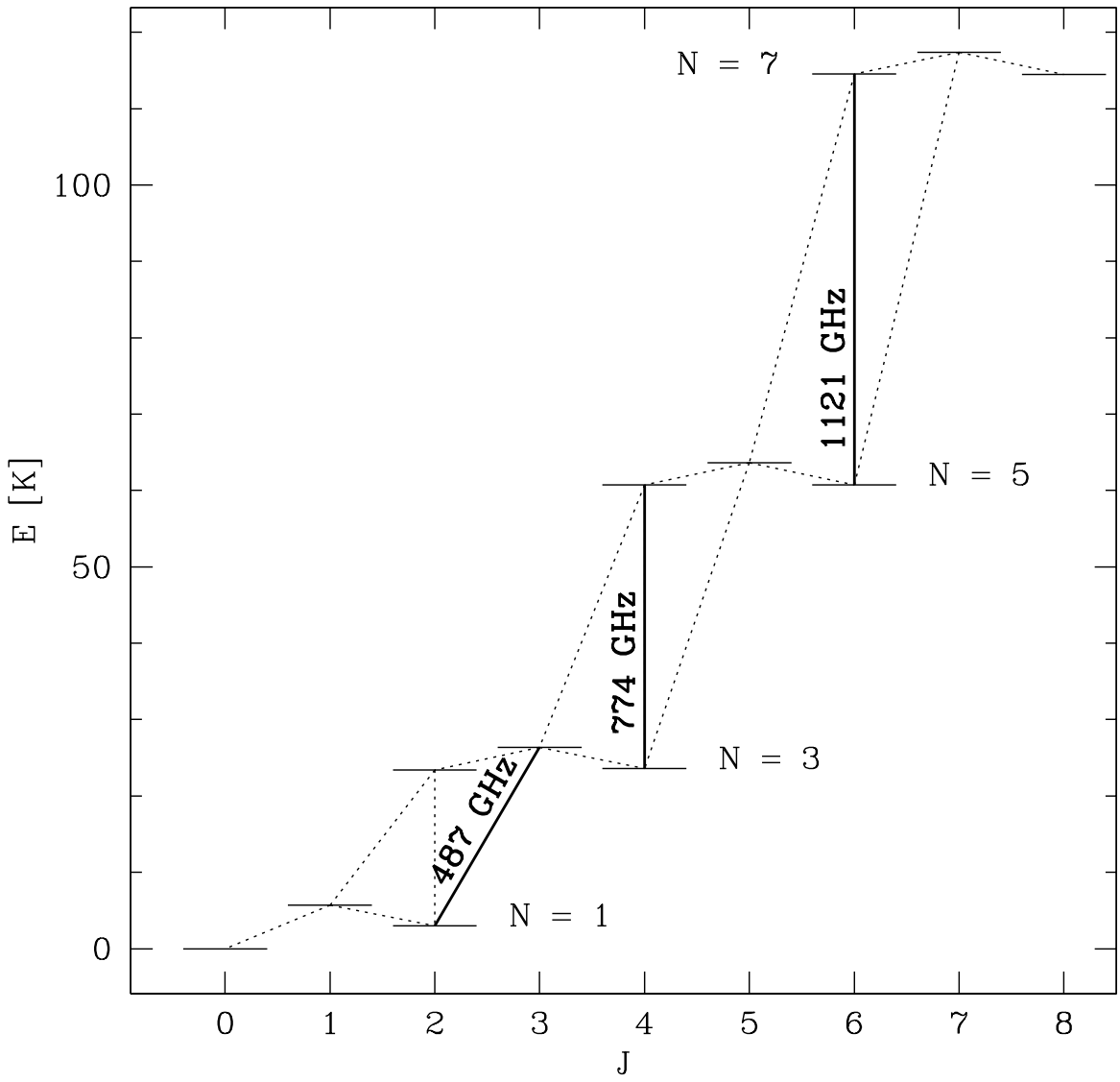

Figure 3.2: Rotational levels of the $X^3\Sigma_g^-$ ground state of O_2. The heavy lines represent the 487 MHz ($3_3 - 1_2$), the 774 MHz ($5_4 - 3_4$), and the 1121 MHz ($7_6 - 5_6$) lines.

CHAPTER 4

COMPUTATIONAL MODELS

4.1 Line intensity calculations

4.1.1 Equations of statistical equilibrium

To calculate the line intensities, it is first necessary to solve the radiative transfer equation; the escape probability method due to Sobolev is an approximation to this. To get the populations of the individual levels, we would solve a set of coupled differential equations:

$$\frac{\partial f_i}{\partial t} = \sum_j f_j(A_{ji}\beta_{ji} + C_{ji}) - f_i \sum_j A_{ij}\beta_{ij} + C_{ij} \tag{4.1}$$

where A_{ij} are the spontaneous emission rates (Einstein A coefficient),[1] β_{ij} are the escape probabilities, C_{ji} are the collisional de-excitation rates, and C_{ij} are the collisional excitation rates. Note that $C_{ji} = nc_{ji}$, where n is the number density of the collision partner and c_{ji} are the collisional de-excitation coefficients. Under the assumption of statistical equilibrium, we can set the left hand side of equation 4.1 to zero (Kaufman and Neufeld [KN96a]). The system of differential equations then becomes a system of linear, coupled, algebraic equations. These equations reflect the equilibrium between atoms (or molecules) moving to higher energy levels due to collisions, balanced against atoms moving to lower energy levels due to collisions as well as to spontaneous emission. For densities greater than the critical density ($n_{cr} = A_{ji}/c_{ji}$), the level populations are in local thermodynamic equilibrium (LTE),

[1] The absence of terms involving B_{ji}, the stimulated emission rates (Einstein B coefficients) arises from the assumption that there is no significant contribution from the ambient radiation field.

which implies that the process is dominated by collisions, with little or no effect on the level populations from from radiative transitions.

To assure a unique non-trivial solution, it is necessary to replace one of the equations with the conservation equation

$$\sum_{j=1}^{l} f_j = 1 \tag{4.2}$$

where l is the total number of energy levels considered. Then the intensity of a single line is

$$I_\nu = \frac{1}{2\pi} \int \Lambda_\nu dz \tag{4.3}$$

where

$$\Lambda_\nu = f_i n(M) \Delta E_{ij} A_{ij} \beta_{ij}. \tag{4.4}$$

Λ_ν is the cooling rate, $n(M)$ is the number density of the emitting species, f_i is the level fraction for the upper level of the transition, ΔE_{ij} is the energy difference between the upper and lower levels of the transition, A_{ij} is the probability for the transition (the Einstein A coefficient), and β_{ij} is the probability that the emitted photons "escape" from each dz thick slice of the cloud. The factor $\frac{1}{2\pi}$ arises from the fact that the emitted photons emerge only through the front surface.
(Tielens [Tie05].)

4.1.2 Escape probability

The factor β in equations 4.1 and 4.3, is the probability that photons escape the emitting region without being re-absorbed. It is a function of optical depth for a given emission line. Hummer & Rybicki [HR82] derived exact expressions for the escape probability of photons emitted in a planar geometry for both static and

moving media. For moving media, Kaufman and Neufeld [KN96a] made the approximation

$$\beta_{ij} = \frac{1}{1 + 3\tau_S} \tag{4.5}$$

where τ_S is the Sobolev optical depth.

4.2 C-shocks: model

Kaufman and Neufeld [KN96b] developed a C-shock model which treats neutral species and ions (mainly charged dust grains) as separate, weakly coupled fluids through a set of hydrodynamics equations. The model was then applied to shocks of high density ($n = 10^7$–$10^{9.5}$) with shock velocities up to 45 km s^{-1} to successfully reproduce observed water maser emissions. This model has also been used successfully to match observed molecular hydrogen and CO emissions from the Orion-KL region; in [KN96a], predictions for water line emissions from shocked gas at lower densities and velocities were made. We have now applied this model to [O I] and O_2 emission from magnetohydrodynamic C-shocks, as described in later sections.

As pointed out in Section 2.2, O_2 can exist within a limited range of physical conditions. If the temperature rises above ∼400 K, H_2O is formed very readily. Figure 4.1 depicts this effect quite clearly. At low velocities ($\lesssim$ 10km s^{-1}), the temperature is too low for the formation of OH, a necessary precursor to O_2 formation; at high velocities, the temperature is high and oxygen is driven into H_2O. One can see quite clearly the optimal regime for O_2: for v_s ∼10 km s^{-1}, the gas reaches temperatures high enough to initiate OH and then O_2 formation. At v_s ∼20 km s^{-1}, the gas gets warm enough to force essentially all O into H_2O. The O_2 column density peaks at $\sim 10^{17}$ cm^{-2} for $v_s \sim$ 10–12 km s^{-1}. This result justifies

limiting our model to low pre-shock densities (below $n = 10^6$ cm^{-3}) and pre-shock shock velocities (v_s below 20 km s^{-1}).

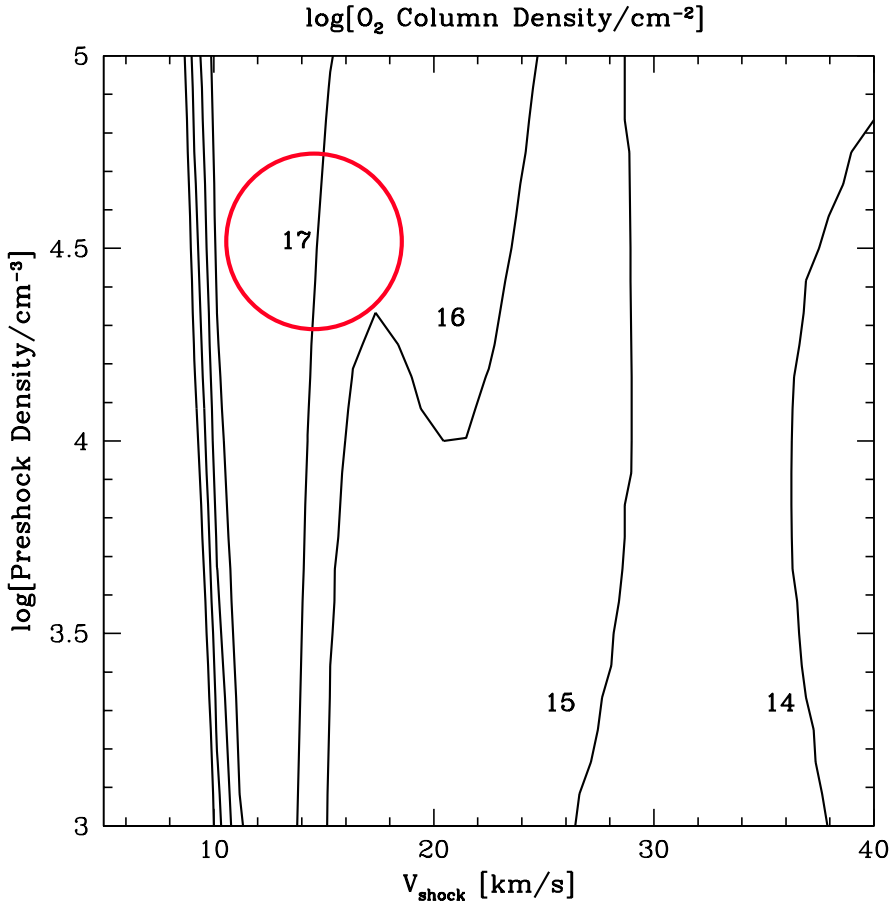

Figure 4.1: O_2 column density as a function of pre-shock density and shock velocity. The red circle indicates the "sweet spot" for O_2 abundance. Figure provided by Michael J. Kaufman (private communication).

4.3 Shocks: escape probability method

As mentioned earlier, the escape probability β_{ij} is approximated by equation 4.5. In the case of a C-Shock, the Sobolev optical depth, τ_S, is related to

the velocity gradient by (Kaufman [KN96a]),

$$\tau_S = \frac{\lambda_{ij}^3}{8\pi|dv/dz|} n(M) A_{ij} \left(\frac{g_i}{g_j} f_j - f_i \right) \tag{4.6}$$

A large velocity gradient results in a small τ_S which, in turn, results in a high escape probability. The physical explanation for this is that if, even in a dense cloud where an emitted photon might be immediately absorbed by a neighboring molecule, the velocity gradient is sufficient to doppler-shift a line more than one line-width (lines have width as a consequence of thermal kinetic energy).Thus photons can escape.

4.4 Implementation

Line intensity calculations were made using programs written in Fortran 90. Rate coefficients for [O I] and [C II] calculations were taken from Table 4 of Tielens and Hollenbach [TH85]. While there may be more recent values available, these values are appropriately used for comparison of our results with those presented in the paper. The primary motive was to verify the correctness of the code and the accuracy of the calculations before using a similar code for the O_2 calculations.

Lique [Liq10] presents the most recent calculation of the de-excitation rate coefficients of the O_2 ($X^3\Sigma_g^-$) fine structure and their temperature dependence, using He as the collision partner. These data, along with level energies and the spontaneous emission rates, have been incorporated into the RADEX database (Schöier, et al. [SvvB05]), scaled by the collisional cross-section ratio $\sigma(H_2)/\sigma(He) \approx 1.37$ to approximate the rates using H_2 as the collision partner. We use these rates for our O_2 calculations.

Calculation of the energy level fractions is as follows: The de-excitation rate coefficient, spontaneous emission rate, and level energy data (RADEX file "02.dat") are read into appropriate data structures. The rate matrix $\boldsymbol{C}$ is then constructed by

interpolating the c_{ji}'s between discreet $c_{ji}(T)$ values and computing the c_{ij}'s, the collisional excitation coefficients:

$$c_{ij} = c_{ji}\frac{g_j}{g_i}e^{-(E_j-E_i)/kT} \tag{4.7}$$

where g_j and g_i are the upper and lower level degeneracies, and E_j and E_i are the upper and lower level energies. The spontaneous emission rate matrix $\boldsymbol{A}$ is then constructed; finally, the statistical equilibrium equation coefficient matrix $\mathbf{M}$ is constructed:

$$M_{ij} = \begin{cases} A_{ji} + C_{ji} & i < j \\ -\sum_{k\neq i} C_{ik} - \sum_{k<i} A_{ik} & i = j \\ C_{ji} & i > j \end{cases} \tag{4.8}$$

replacing the first row (M_{1j}) with all 1's (the conservation equation coefficients). The column vector $\mathbf{v}$ is $\mathbf{0}$ except for $v_1 = 1$. The column vector $\boldsymbol{f}$ is the vector of unknown level fractions, f_i. The system of equations, so constructed, is then solved for $\boldsymbol{f}$:

$$\begin{aligned} \boldsymbol{M}\boldsymbol{f} &= \boldsymbol{v} \\ \boldsymbol{f} &= \boldsymbol{M}^{-1}\boldsymbol{v} \end{aligned} \tag{4.9}$$

using the library function *dgesv* contained in the standard MacOS X framework *vecLib*. To compute the intensities, Equation 4.3 is evaluated using the trapezoidal rule for numerical integration.

For the purpose of comparison of the predicted intensities to the those observed with the *Herschel* HIFI instrument, the resulting intensities are then converted to units of $\int T dv$. For a single line,

$$I_\nu^{model} = \int T dv = \frac{c^3}{2\nu^3 k}10^{-5}\int_{\delta(\nu)} I_\nu d\nu \tag{4.10}$$

where T is the "antenna temperature". This is a term from radio astronomy referring to the power into the receiver, $kTdv$. T, the antenna temperature, is the temperature to which a hypothetical resistor placed across the antenna output would be raised due to the power input. See Garrett's lecture [Gar10] for a clear, but detailed discussion.

4.5 Resulting predicted emissions

4.5.1 Emission from [O I] and [C II] transitions

As a verification of the accuracy of the level population and intensity calculation codes, a plot was made of the ratio of intensities of the [O I] 145 μm and 63 μm lines as a function of temperature, based on the fine-structure data given in Tielens [TH85]. The result, shown in Figure 4.2, closely matches the plot in [TH85].

As further verification, we plotted the cooling in the [C II] 158 μm line, as a function of temperature and density, based on the fine-structure data given in Tielens [TH85]. This result, shown in Figure 4.3, also matches the similar plot in [TH85]. C II is a two-level system, having a single transition from the upper level ($^2P_{3/2}$) to the lower level ($^2P_{1/2}$), and the cooling rate is just Λ_ν, as calculated using equation 4.4. Since this line is optically thin, $\beta_{esc} = 1$.

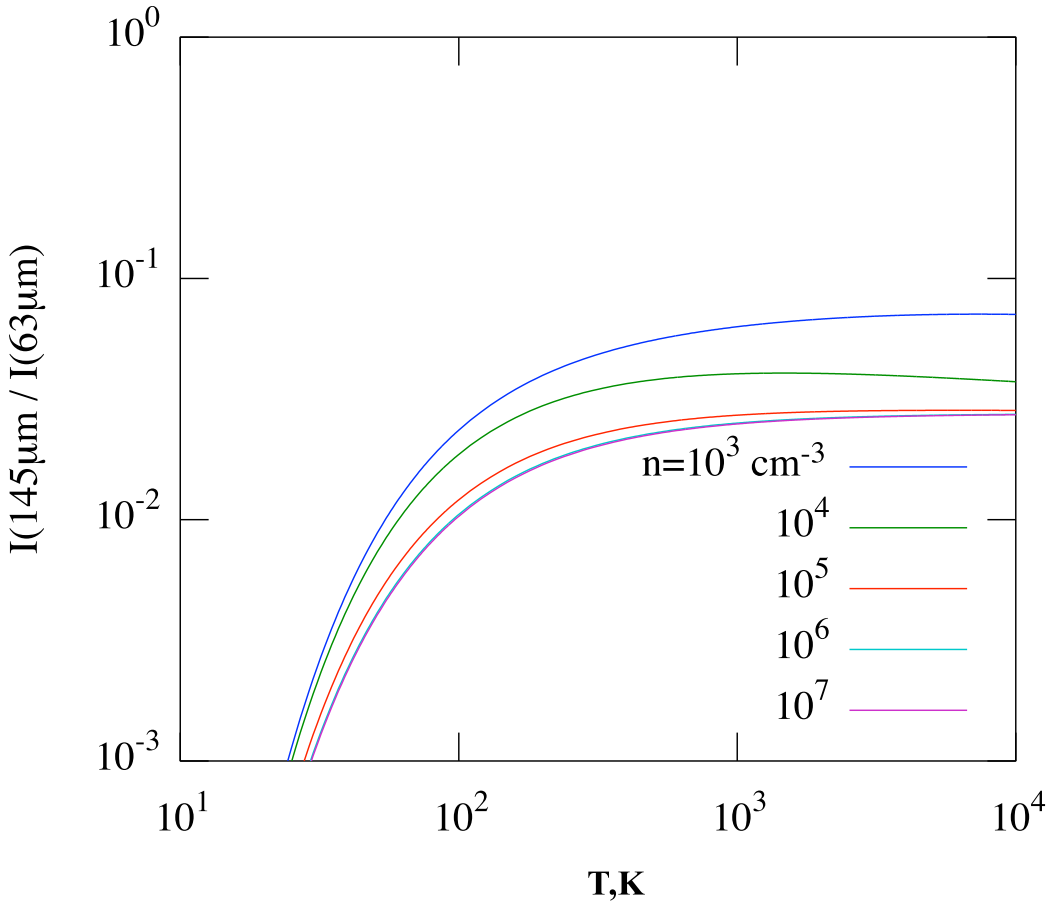

Figure 4.2: Ratio of intensity of [O I] 145 μm and 63μm lines as a function of temperature.

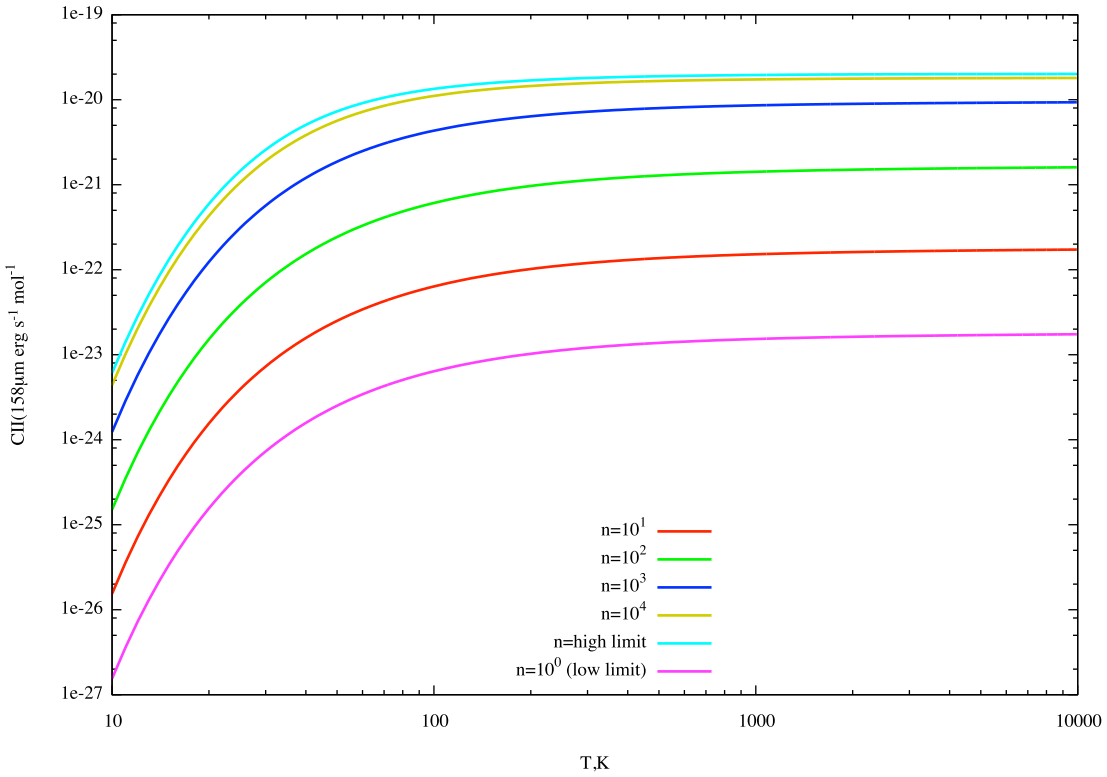

Figure 4.3: Cooling in the [C II] 158μm line, as a function of temperature and density.

4.5.2 Emission from shocked [O I] transitions

In order to calculate emission from shocked O I, we use M. Kaufman's magnetohydrodynamic (MHD) shock model to generate the profile data: depth, density of the collision partner (H_2), temperature, and abundance of oxygen (O). From this data, we calculate the level fractions, using Equation 4.1 (with $\beta = 1$), then we calculate τ_S, using Equation 4.6. To get the required velocity gradient, we first recover the velocity from the profile data using the continuity equation

$$\rho v = \rho_0 v_0 \Rightarrow nv = n_0 v_0 \text{ which gives}$$

$$(n_0 + \Delta n)(v_0 + \Delta v) = nv = n_0 v_0$$

Dropping the second order term and solving for v,

$$\Delta v = -v_0 \Delta n / n_0 \text{ or}$$
$$v(z + \Delta z) = v(z) - \frac{v(z)}{n(z)}(n(z + \Delta z) - n(z)) \tag{4.11}$$

where v_0 and n_0 are the initial conditions for the profile data. The velocity gradient is then computed by numerically differentiating $v(z)$ with respect to z. τ_S and β_{ij} are then computed at each depth in order to find Λ_ν, the cooling rate, which is then numerically integrated to get the flux.

Results from computations on profile data for which $v_0 = 15\text{km s}^{-1}$ and $n_0 = 10^3$ cm^{-3} are shown in the Figures 4.4a through 4.7b. The temperature plot is repeated three times in order to illustrate how abundance depends on temperature; temperature on the velocity gradient (in turn dependent on density, as implied by equation 4.11); and finally the cooling rate on temperature (and abundance). The flux is computed by integrating the cooling rate over z, the cloud depth. As shown in Figure 4.7a, the emergent flux reaches a constant level as the cooling rate (Figure 4.6a) falls off.

The last plot, Figure 4.7b, yielded an interesting surprise: τ_S suddenly drops then disappears in the [O I] 145 μm line over the shock zone, that is, τ_S becomes negative. Equation 4.6 shows us why: τ_S becomes negative when $\frac{f_i}{f_j} > \frac{g_i}{g_j}$; in other words, a population inversion has taken place. We have predicted masing activity in the [O I] 145 μm line over the shock zone. Alas, this is not new—Liseau, et. al. [LJT06] discuss masing activity in the ground state of O I as a possible contributor to an observed line ratio anomaly. Goicoechea, et. al. [GCH09] describe the first detection of the 63 μm line at the edge of the Horsehead photodissociation region, hinting at the possibility of maser action in the 145 μm line, which would impact the intensity ratio.

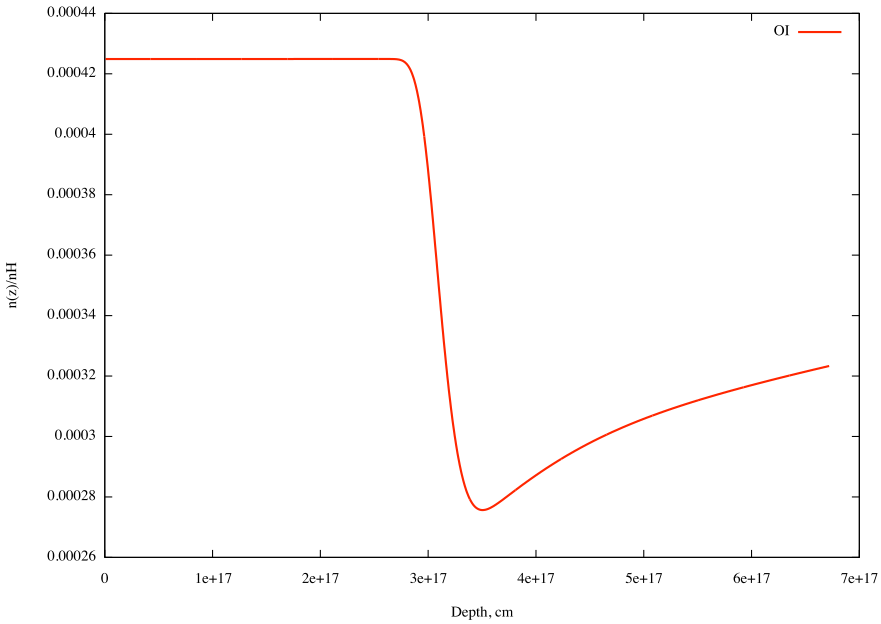

(a) Abundance

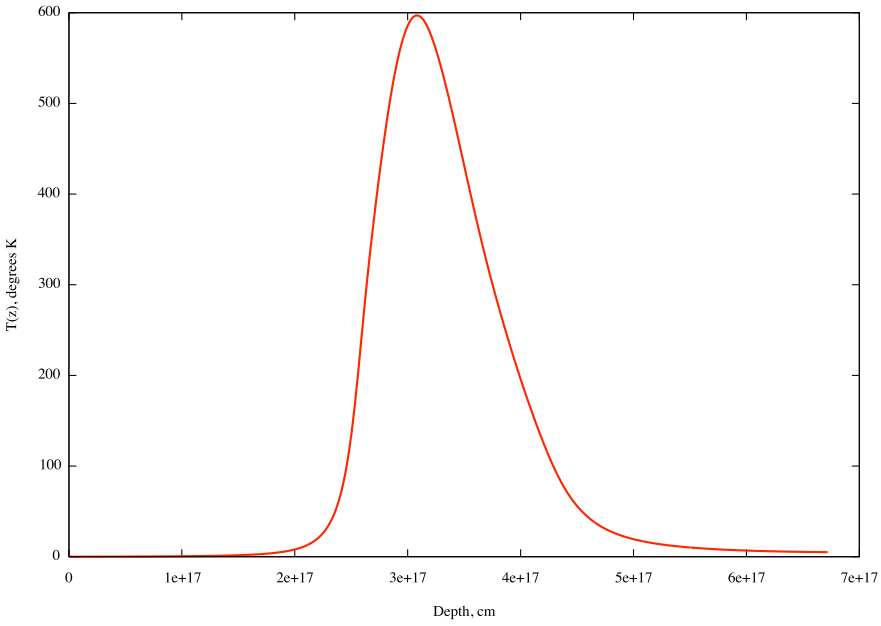

(b) Temperature

Figure 4.4: Abundance of O I and gas temperature as a function of cloud depth in shocked gas. The sharp decrease in abundance of O I as the temperature spikes in the shock zone is mainly due to conversion to H_2O.

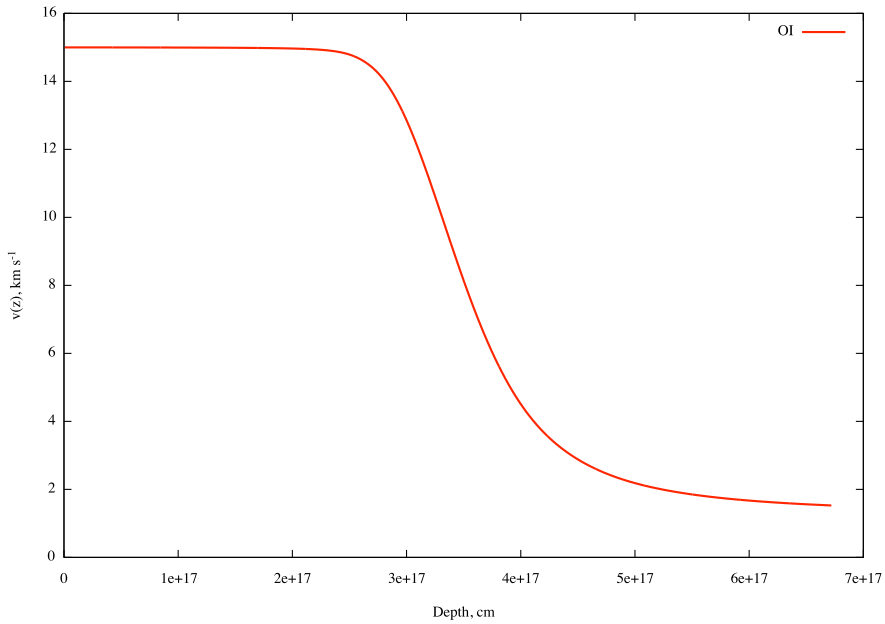

(a) Velocity

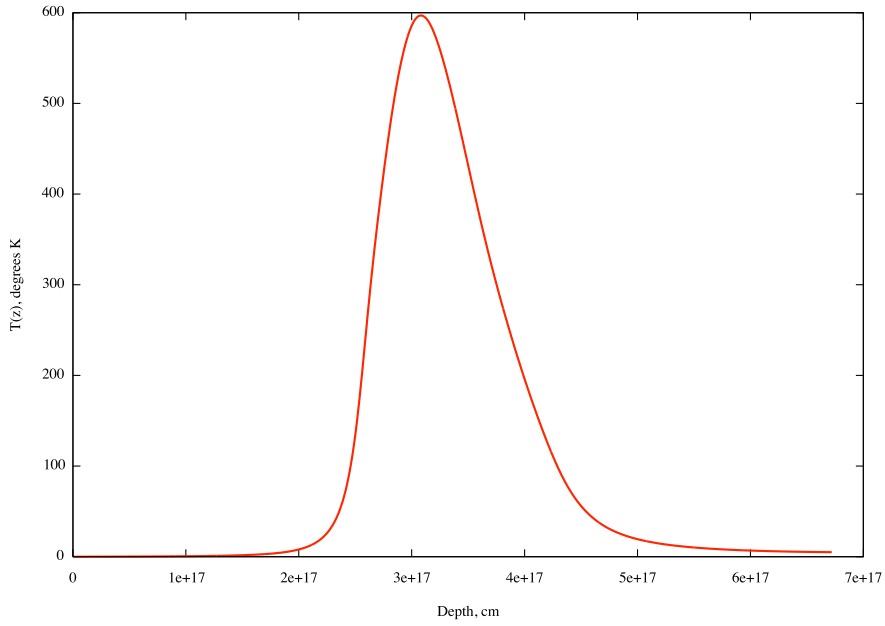

(b) Temperature

Figure 4.5: Velocity and gas temperature as a function of cloud depth in shocked gas. The velocity gradient in the shock zone gives rise to the temperature spike.

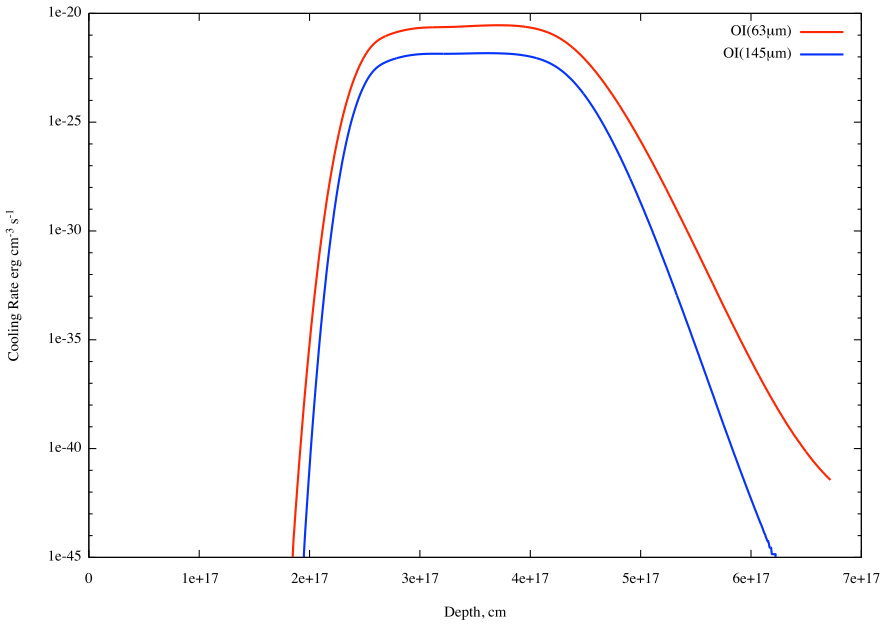

(a) Cooling Rate

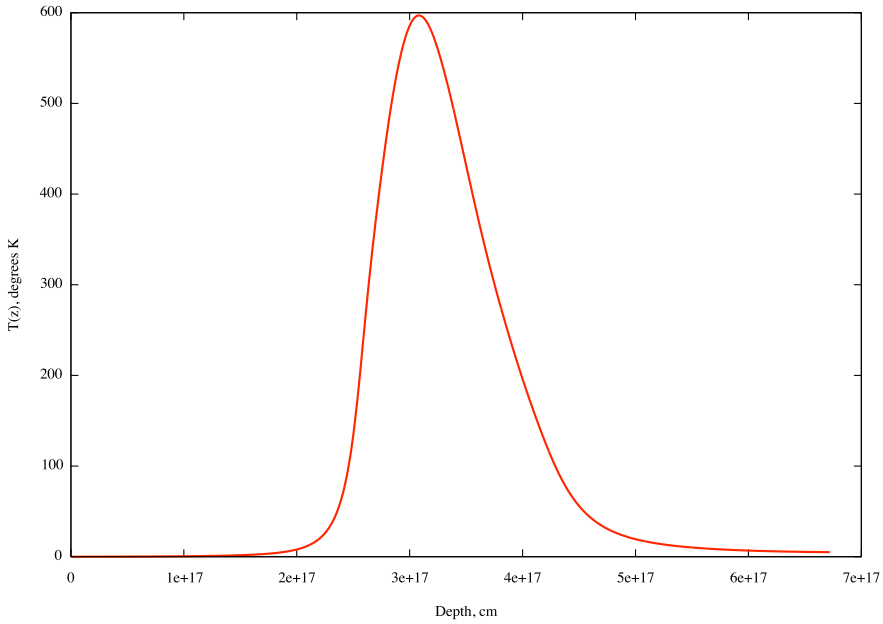

(b) Temperature

Figure 4.6: [O I] 63 μm and 145 μm cooling rates (Λ) and gas temperature as a function of cloud depth. Emission sharply increases with the temperature rise (density is also increasing rapidly) in the shock zone, then falls off past the shock.

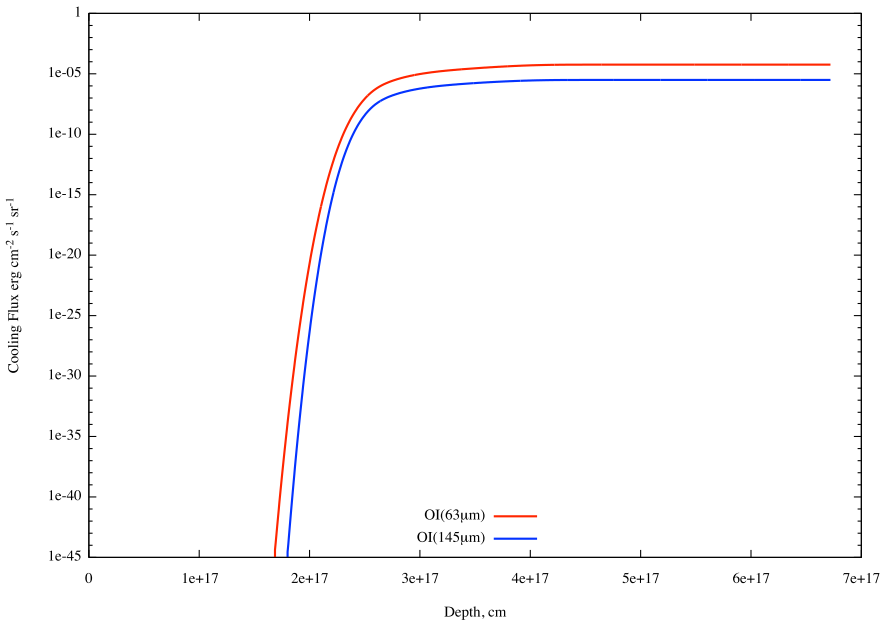

(a) Flux

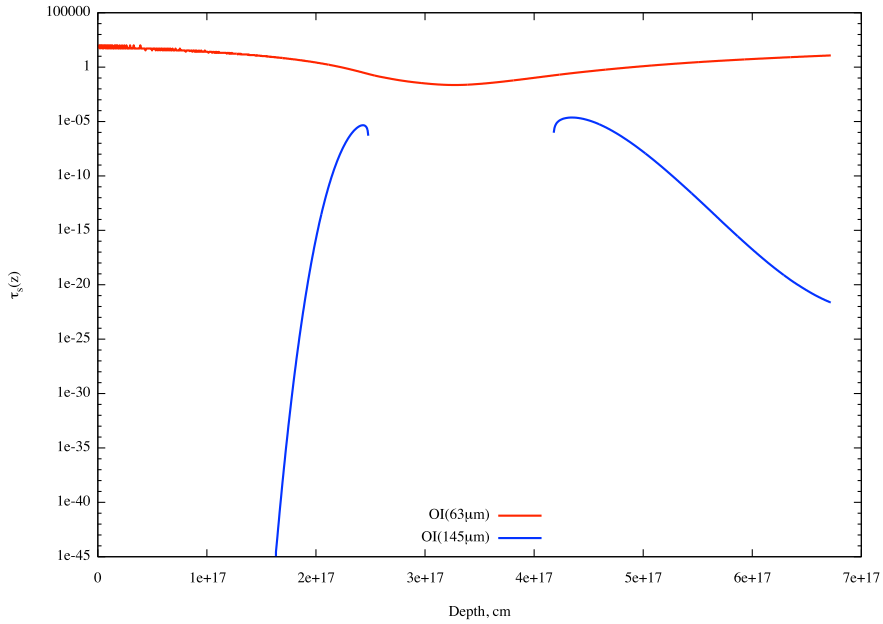

(b) Sobolev optical depth, τ_s

Figure 4.7: (a) Integrated flux from the cloud surface. Flux increases through the shock peak, then approaches a constant value as Λ falls off. (b) Sobolev optical depth in the 63 μm line dips in the shock zone, while optical depth in the 145 μm line turns negative, indicating maser activity in the shock zone.

CHAPTER 5

OBSERVATIONS OF O_2

5.1 Earlier attempts at observation

Direct detection of the main O_2 isotopomer by terrestrial telescopes is not possible, since the emissions are blocked due to absorption in earth's oxygen-rich atmosphere. Attempts to detect unblocked emissions from the rare $^{16}O^{18}O$ isotopomer and a balloon-based search for the main isotopomer have also failed (Pagani, et al. [PPM$^+$99]).

Clearly, the best opportunity for observation of molecular oxygen comes from the use of space telescopes with instrumentation operating in the submillimeter range of the lower rotational transitions of O_2. The *Submillimeter Wave Astronomy Satellite (SWAS)*, described by Melnick, et al. [MSA$^+$00], was used to make observations of a variety of sources in the 487 MHz line, with no convincing detections (Goldsmith, et al. [GMB$^+$00]). Other observations using *SWAS* and *Odin* have likewise proven disappointing, and indicate a very low abundance ($\lesssim 1$ % of prediction of gas-phase theory) of molecular oxygen (Goldsmith, et al. [GLB$^+$11]). It may be that the prevalence of molecular oxygen really is lower, or that other explanations may exist, including beam dilution and low sensitivity of older instrumentation.

5.2 Recent observations: The Herschel Oxygen Project

The Heterodyne Instrument for the Far-Infrared (HIFI) (de Graauw, et al. [dHP$^+$10]), launched on the *Herschel Space Observatory* (Pilbratt, et

al. [PRP$^+$10]) in May 2009,[1] provides greatly improved spatial resolution and increased sensitivity, and covers the 480-1250 GHz range (See de Graauw, et al. [dHP$^+$10]). The Open Time Key Program Herschel Oxygen Project (HOP) team carried out observations of Orion using the HIFI instrument in the three bands covering the 487, 774, and 1121 GHz lines of O_2 (Goldsmith, et al. [GLB$^+$11]) on five different operational days, confirming emission from O_2.

5.2.1 HIFI observations of 487, 774, and 1121 GHz lines of O_2

The HOP team identified three rotational transitions of O_2 in the H_2 Peak 1 outflow of the Orion Molecular Cloud through observations with HIFI. See Table 5.1 for the integrated main beam intensities ($\int T_{mb} dv$) of the three lines and their statistical uncertainties, as adapted from Goldsmith, et al. [GLB$^+$11]. See also the observed spectra in Figure 5.1 which give rise to the data in Table 5.1.

The authors then plotted the intensity ratios, I_{487}/I_{774} and I_{1121}/I_{774} assuming LTE populations and equal beam filling factors for all transitions.

Fig 5.2 shows similar plots to those using the LTE calculation, with the addition of curves using non-LTE calculations at two different densities, confirming that these densities produce ratios close to the LTE calculation. The beam intensity ratios are:

$$\frac{\int (T_{mb} dv)_i}{\int (T_{mb} dv)_j} = \frac{\Lambda_i}{\Lambda_j} \left(\frac{\nu_j}{\nu_i} \right)^3 . \tag{5.1}$$

For LTE calculations, Λ_i is given by:

$$\Lambda_i = \frac{g_i e^{-E_i/T}}{\sum_n g_n e^{-E_n/T}} A_{ij} \Delta E_{ij} \tag{5.2}$$

where g_i is the degeneracy of the upper energy level, A_{ij} is the Einstein spontaneous

[1] *Herschel* is an ESA space observatory with science instruments provided by European-led Principal Investigator consortia and with important participation from NASA.

emission coefficient for the transition, ΔE_{ij} is the transition energy, and the denominator is the partition function. For non-LTE calculations, the system of statistical equilibrium equations for the first 36 levels are solved to get the level populations f_i. Then

$$\Lambda_i = f_i A_{ij} \Delta E_{ij} \beta_{esc} \tag{5.3}$$

where (for O_2) $\beta_{esc} = 1$.

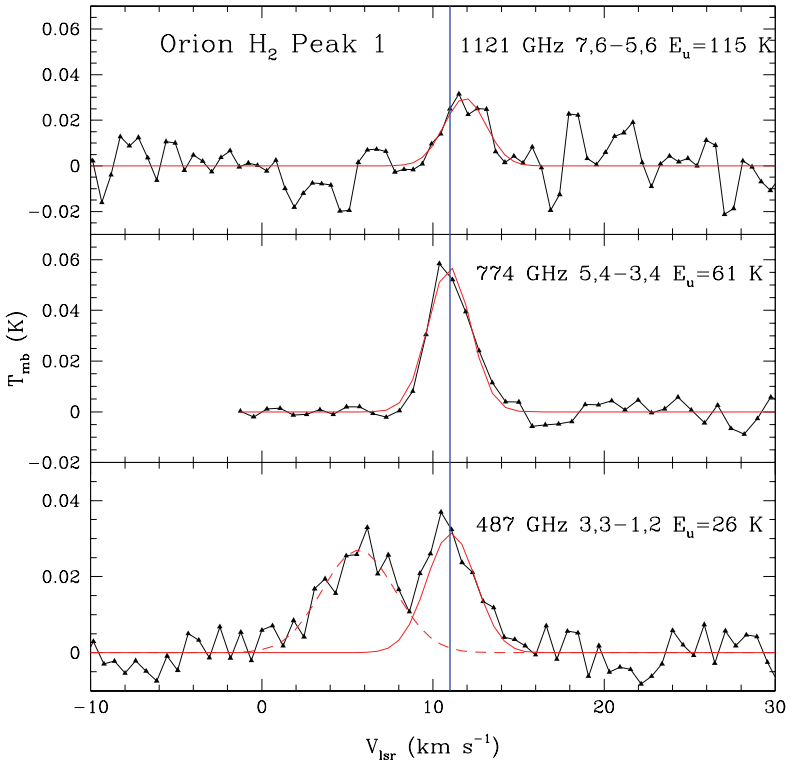

Figure 5.1: Spectra observed with the *Herschel* HIFI instrument. The red lines are the fitted Gaussians used for Table 5.1 Figure used with the kind permission of Michael Kaufman and the AAS [GLB+11].

Table 5.1: Observed O_2 Lines (adapted from [GLB+11] with permission of Michael Kaufman and the AAS)

Transition	Frequency (GHz)	$\int T_{mb} dv$ (K km s^{-1})†
3,3-1,2	487.249	$0.095 \pm .011$
5,4-3,4	773.840	$0.177 \pm .008$
7,6-5,6	1120.715	$0.091 \pm .018$

† Only values for the feature at $V_{lsr} \approx 11$ km s^{-1} included.

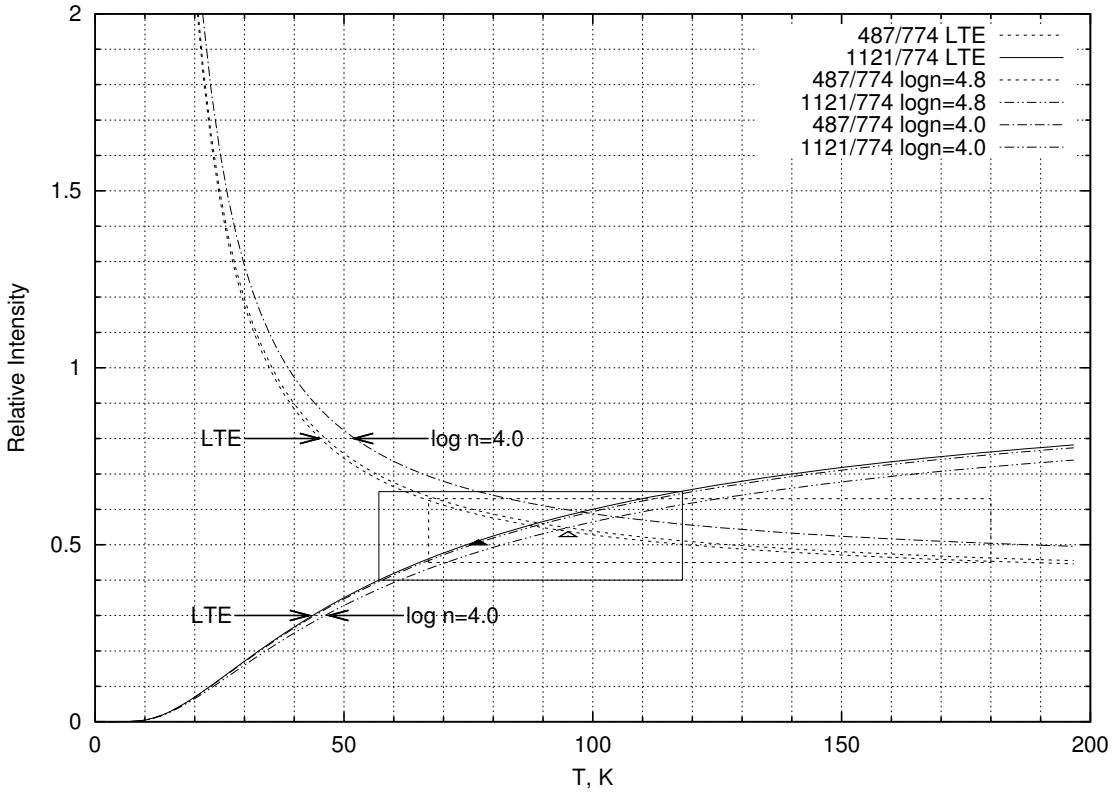

Figure 5.2: Computed ratios of intensities of the O_2 487 GHz to 774 GHz lines and of the 1121 GHz to 774 GHz lines, using LTE calculations and non-LTE calculations for two densities. The boxes delineate the error limits of the ratios of the measured intensities; the triangles point to the ratios of the mean values from Table 5.1.

5.3 Applying the model

5.3.1 Intensity calculations

The computational results from M. Kaufman's magnetohydrodynamic shock model code [KN96a], consisting of temperature, density of molecular hydrogen $n(H_2)$ and molecular oxygen abundance $x(O_2)$, as a function of cloud depth, were used to calculate the level fractions using the scheme described in section 4.4. The

intensities were then computed using equation 5.3.

These three lines have very low spontaneous emission rates ($\sim 10^{-8}$ s^{-1}) and are, therefore, optically thin in typical astrophysical environments. For this reason, we may set $\beta = 1$ everywhere. To verify this this claim, equation (B12) from Tielens [TH85] was used to get the column density of hydrogen at which the optical depth reaches unity:

$$N_\tau(\nu_{ij}) = \frac{8\pi\delta v_d}{A_{ij}\lambda_{ij}^3}\frac{g_j}{g_i}\frac{1}{x(O_2)}, \tag{5.4}$$

where δv_d is the doppler width of the given line and $x(O_2)$ is the relative abundance of molecular oxygen. Using values of 3.05 km s^{-1}, 2.91 km s^{-1}, and 2.87 km s^{-1}, for the doppler width of the 487 HHz, 774, and 1121 GHz lines, respectively, and $x(O_2)$ of 3.80×10^{-6}, $N_\tau \approx 10^{24}$ cm^{-2} for the three lines; the estimates made by Goldsmith, et al. [GLB$^+$11] for N(H_2) were in the range 8.9×10^{21} cm^{-2} to 2.1×10^{23} cm^{-2}. Since these column densities are less than the N_τ values, optical depth is not important and our assumption of nearly unity escape probability is valid.

Line intensities for each of the three lines were then calculated using equation 4.3 above, then computing the integrated beam intensities using equation 4.10.

5.3.2 Intensity ratios and beam filling factor

Assuming a source on boresite (direct line-of-sight between source and receiver),

$$I_{\nu_i}^{obs} = I_{\nu_i}^{src}\, ff_{\nu_i} \tag{5.5}$$

where $I_{\nu_i}^{obs}$ is the observed intensity, $I_{\nu_i}^{src}$ is the source intensity, and ff_{ν_i} is the beam filling factor for the given frequency. The beam filling factor is the fraction of the beam occupied by the source. See Figure 5.4, for example. If the source size is larger than the detector beam size (i.e., fully resolved) then $ff = 1$. If the source

size is smaller (or equal) to the detector beam size, then ff is the ratio of the source size to the beam size:

$$ff_{\nu_i} = \begin{cases} \Omega^{src}_{\nu_i}/\Omega^{beam}_{\nu_i} & \Omega^{src}_{\nu_i} \leqslant \Omega^{beam}_{\nu_i} \\ 1 & \Omega^{src}_{\nu_i} > \Omega^{beam}_{\nu_i} \end{cases} \tag{5.6}$$

The intensity ratios are then

$$\frac{\left(\int Tdv\right)^{obs}_{487}}{\left(\int Tdv\right)^{obs}_{774}} = \frac{F^{model}_{487}}{F^{model}_{774}} \left(\frac{773.840}{487.249}\right)^3 \frac{ff_{487}}{ff_{774}} \text{ and,} \tag{5.7}$$

$$\frac{\left(\int Tdv\right)^{obs}_{1121}}{\left(\int Tdv\right)^{obs}_{774}} = \frac{F^{model}_{1121}}{F^{model}_{774}} \left(\frac{1120.715}{487.249}\right)^3 \frac{ff_{1121}}{ff_{774}}. \tag{5.8}$$

We use ratios of intensities since factors common to all frequencies, such as pointing offset error, are canceled out, simplifying comparisons.

5.3.3 An alternative to the "equal beam filling factor" assumption

The full-width half-maximum beam widths for the HIFI instrument are 44″, 28″, and 19″ for the 487 GHz, 774 GHz, and 1121 GHz beams, respectively (Pilbratt, et al. [PRP+10]). The observed intensity ratios, based on Table 5.1, are

$$0.45 \leqslant \frac{\left(\int Tdv\right)^{obs}_{487}}{\left(\int Tdv\right)^{obs}_{774}} \leqslant 0.63 \text{ and } 0.40 \leqslant \frac{\left(\int Tdv\right)^{obs}_{1121}}{\left(\int Tdv\right)^{obs}_{774}} \leqslant 0.65. \tag{5.9}$$

If it is assumed that the source fills all the beams, then equation (5.8) gives values that fall well outside the statistical uncertainty limits of the observed I_{1121}/I_{774} ratio (See Figure 5.3 (a)). However, if it is assumed that the source completely fills the 1121 GHz beam, but not the others, an effective source diameter can be determined which does result in values falling inside the limits (See Figure 5.3 (b) and Figure 5.4).

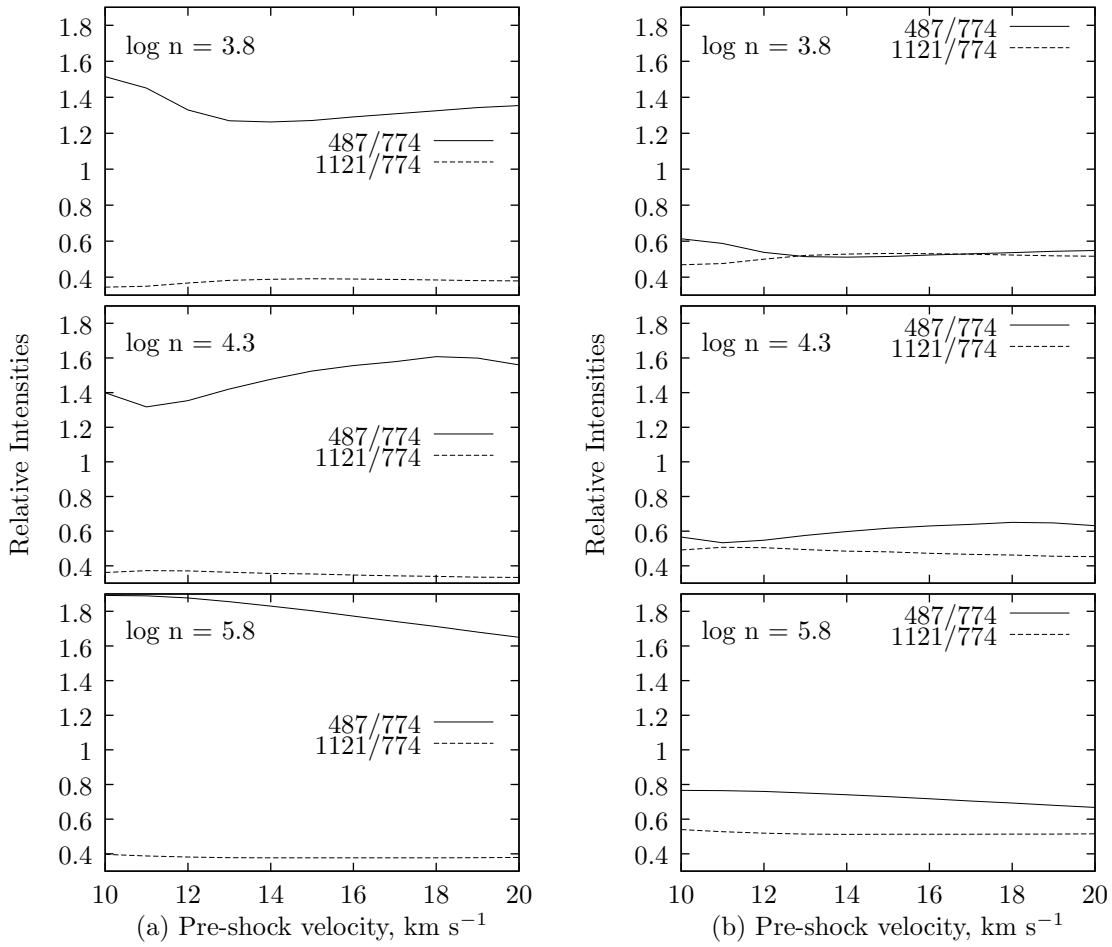

Figure 5.3: Computed ratios of intensities of the O_2 487 GHz to 774 GHz lines and of the 1121 GHz to 774 GHz lines for three values of n(H_2) for the range of pre-shock velocities between 10 and 20 km s^{-1}, (a) assuming all beams filled, and (b) assuming a source diameter of 24″. Note that the computed relative intensities fall completely outside the range of observed relative intensities unless only the 1121 GHz beam is filled.

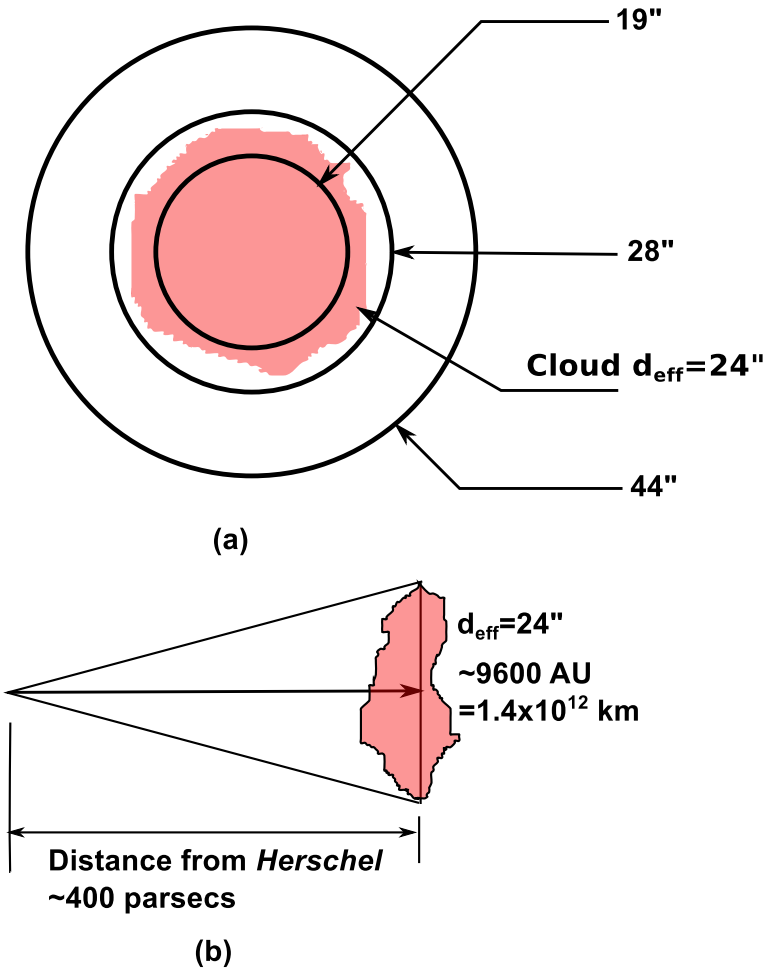

Figure 5.4: Schematic of best-fit filling factors. (a) Cloud emission fills 19″ (1121 GHz) beam, but not the others. (b) Cloud size is roughly 9600 AU.

The solid angle of a beam, Ω, can be expressed as $2\pi(1-\cos\theta) = 2\pi(2\sin^2\theta/2)$, where θ is half the beam diameter; for small θ, $\Omega = 4\pi(\theta/4)^2$. The ratio Ω_i/Ω_j is then $(\theta_i/\theta_j)^2$. For $\theta_{487} > \theta_{774} > \theta_{src} \gtrsim \theta_{1121}$, the beam filling factors and ratios are

$$ff_{1121} = 1, \qquad ff_{774} = \left(\frac{\theta_{src}}{28''}\right)^2, \qquad ff_{487} = \left(\frac{\theta_{src}}{44''}\right)^2,$$
$$\frac{ff_{487}}{ff_{774}} = \left(\frac{28''}{44''}\right)^2, \text{ and} \qquad \frac{ff_{1121}}{ff_{774}} = \left(\frac{28''}{\theta_{src}}\right)^2. \tag{5.10}$$

Contour plots for several values of θ_{src} are shown in Figures 5.5-5.9, displaying only the contours within the uncertainty limits for each ratio. While a number of intersections occur for these ratios, only $23.75 \leqslant \theta_{src} \leqslant 24.25$ produce intersections at the mean values of $I_{487}/I_{774} = 0.54$ and $I_{1121}/I_{774} = 0.51$. Fig 5.7 shows that, at a source diameter of $24.00''$, a pre-shock velocity of 13 km s^{-1} with pre-shock density n(H_2)= 10^4 cm^{-3} reproduces the beam intensity ratios $I_{487}/I_{774} = 0.54$ and $I_{1121}/I_{774} = 0.51$. Fig 5.8 shows that, at a source diameter of $24.25''$, a pre-shock velocity of 15.9 km s^{-1} with pre-shock density n(H_2)= $10^{3.85}$ cm^{-3} reproduces the same ratios. All the figures show other intersections for various other combinations of the beam ratios, all within the observed statistical uncertainty limits of $0.45 \leqslant I_{487}/I_{774} \leqslant 0.63$ and $0.40 \leqslant I_{1121}/I_{774} \leqslant 0.65$. Thus MHD shock models are able to reproduce the observed line ratios under the assumption that pre-shock velocities are in the range 12–16 km s^{-1} and the source diameter is $\sim 24''$.

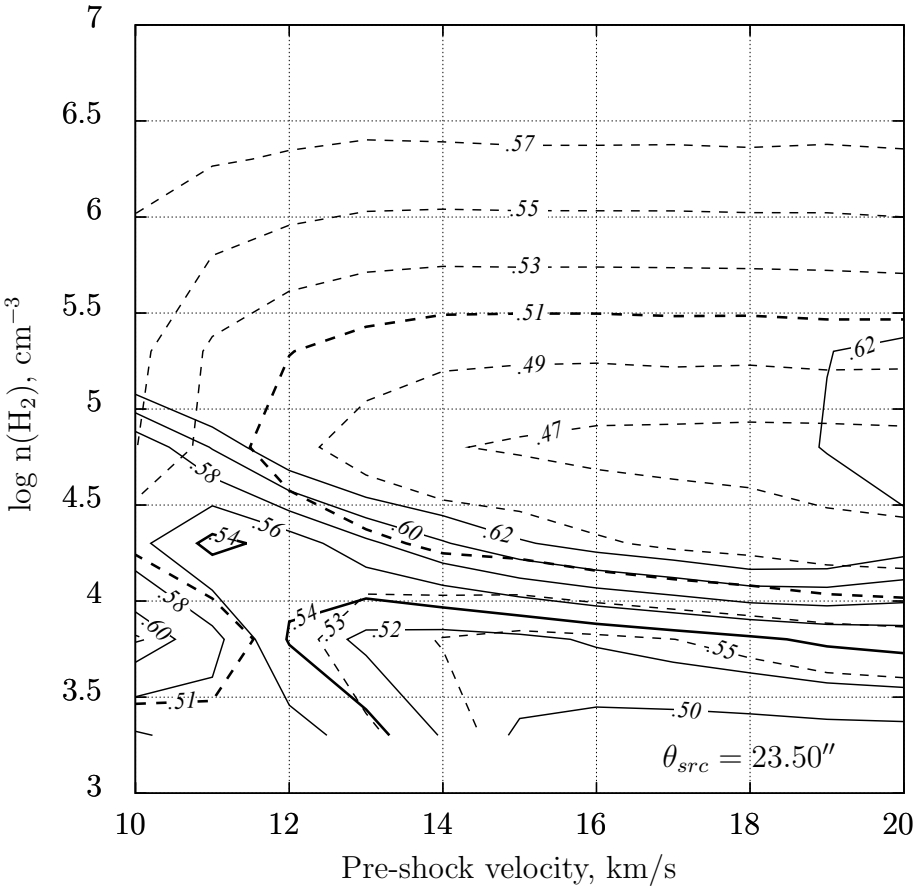

Figure 5.5: Computed ratios of intensities of the O_2 487 GHz to 774 GHz lines and of the 1121 GHz to 774 GHz lines, $\theta_{src} = 23.50''$. Solid lines are I_{487}/I_{774} and dashed lines are I_{1121}/I_{774}. The highlighted lines are the center values, $I_{487}/I_{774} = .54$ and $I_{1121}/I_{774} = .51$. Note that these two contours do not intersect.

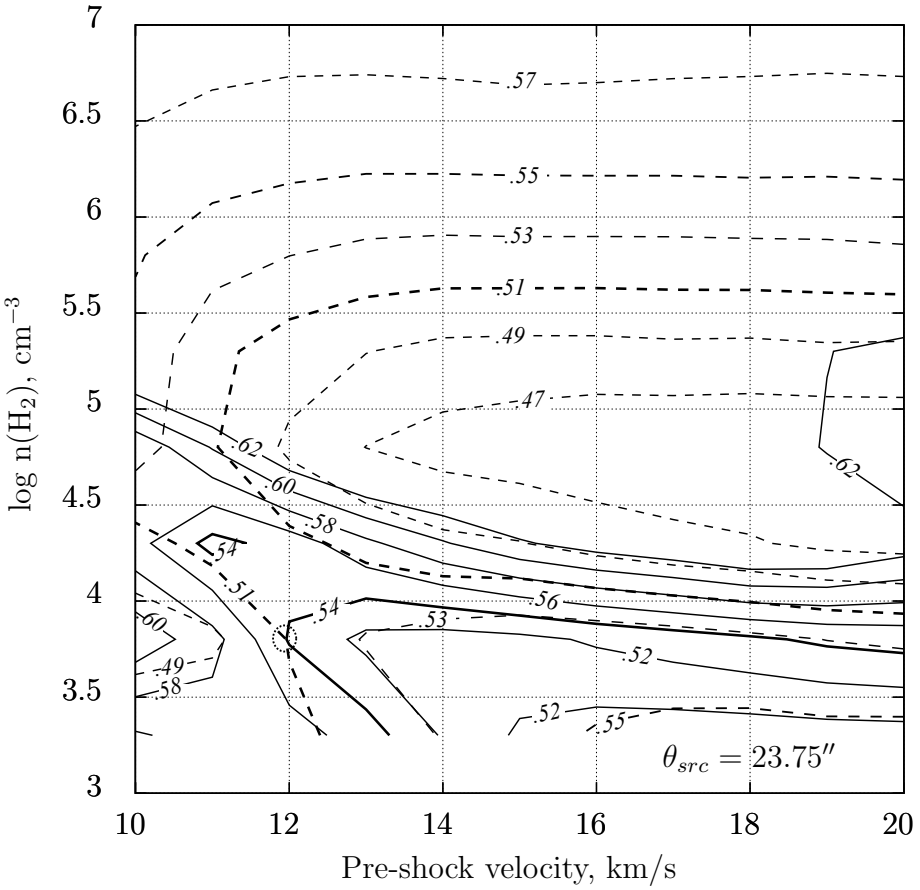

Figure 5.6: Computed ratios of intensities of the O_2 487 GHz to 774 GHz lines and of the 1121 GHz to 774 GHz lines, $\theta_{src} = 23.75''$. Solid lines are I_{487}/I_{774} and dashed lines are I_{1121}/I_{774}. The highlighted lines are the mean values, $I_{487}/I_{774} = .54$ and $I_{1121}/I_{774} = .51$. Note the marked intersection at v = 12 km s^{-1}, n = $10^{3.8}$ cm^{-3}.

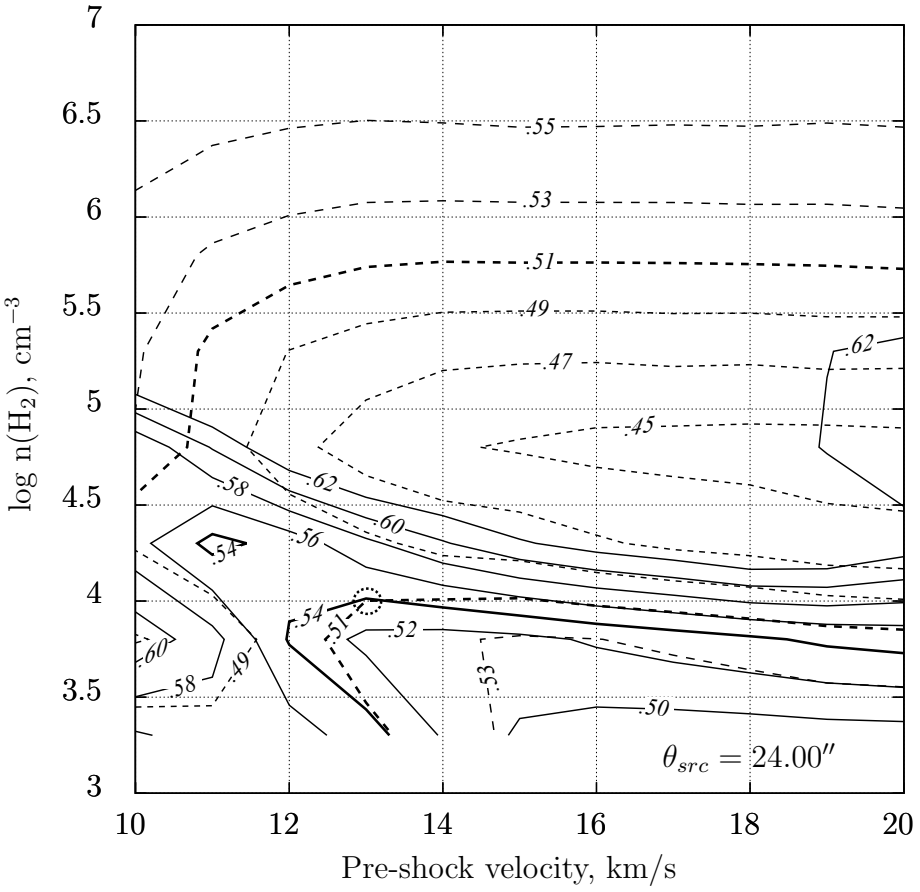

Figure 5.7: Computed ratios of intensities of the O_2 487 GHz to 774 GHz lines and of the 1121 GHz to 774 GHz lines, $\theta_{src} = 24.00''$. The highlighted lines are the mean values, $I_{487}/I_{774} = .54$ and $I_{1121}/I_{774} = .51$. Note the marked intersection at v = 13.2 km s^{-1}, log n = $10^{4.0}$ cm^{-3}.

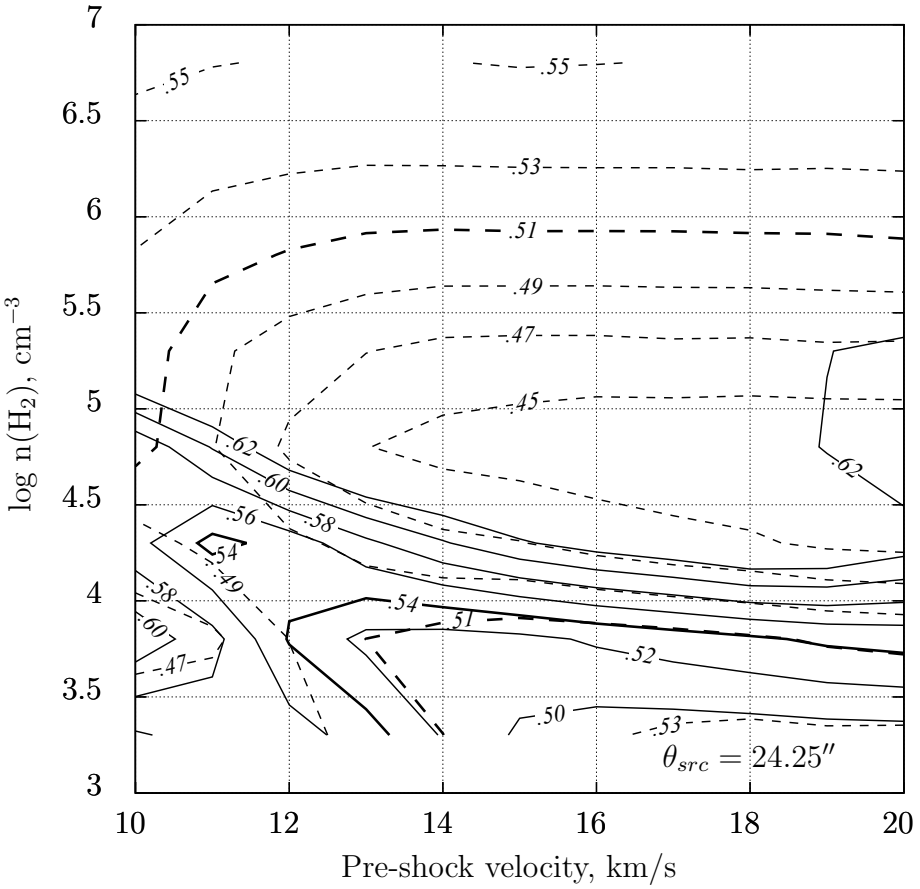

Figure 5.8: Computed ratios of intensities of the O_2 487 GHz to 774 GHz lines and of the 1121 GHz to 774 GHz lines, $\theta_{src} = 24.25''$. The highlighted lines are the mean values, $I_{487}/I_{774} = .54$ and $I_{1121}/I_{774} = .51$. Note that the $I_{487}/I_{774} = .54$ and $I_{1121}/I_{774} = .51$ contours intersect at v = 15.8 km s^{-1}, log n = 3.85 and closely track each other to v = 20 km s^{-1}, n = $10^{3.5}$ cm^{-3}.

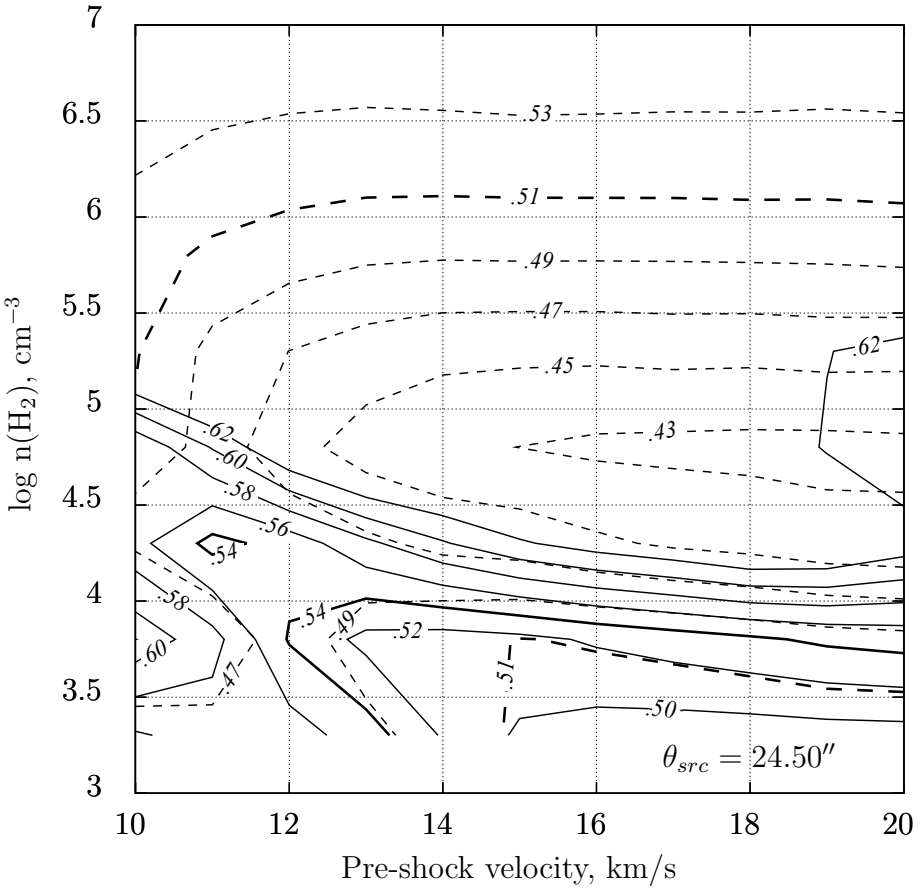

Figure 5.9: Computed ratios of intensities of the O_2 487 GHz to 774 GHz lines and of the 1121 GHz to 774 GHz lines, $\theta_{src} = 24.50''$. The highlighted lines are the mean values, $I_{487}/I_{774} = .54$ and $I_{1121}/I_{774} = .51$. Note that these two contours do not intersect.

CHAPTER 6

CONCLUSIONS

The magnetohydrodynamic (MHD) C-shock model was used to calculate O_2 emission over a range of pre-shock velocities and densities, providing calculated shock profile data, which we then used to calculate relative intensities of the three recently measured rotational lines of O_2. Our calculations produced results consistent with the *Herschel* HIFI measurements reported by the HOP team, assuming that the source completely fills the 1121 GHz beam, but only partially fills the 774 GHz or 487 GHz beams. Assumed source diameters between of 23.75″ and 24.25″ reproduced the measured mean beam intensity ratios $I_{487}/I_{774} = 0.54$ and $I_{1121}/I_{774} = 0.51$ for pre-shock velocities $\sim$ 12–16 km s^{-1}. Our findings suggest either a single source with an effective diameter of $\sim 24''$ emitting in the line of sight, or multiple sources with the same effective diameter.

The actual situation is undoubtedly much more complex, with multiple gas clumps emitting in a range of velocities and densities. Our results further confirmed that O_2 emission is found in shock zones with pre-shock density n$\sim 10^{3.8}$–10^4 cm^{-3} and pre-shock velocities in the range $12 \leq v_s \leq 16$ km s^{-1}. While the effectiveness of the MHD model has previously been demonstrated by Kaufman and Neufeld [KN96a], and Hollenbach and Kaufman [HKBM09] for observations of other species under a variety of conditions, and while our results are certainly reasonable, other methods will need to be explored to confirm our findings for the effective diameter of the source of the reported O_2 emission. Observations of other species in the same region are also needed to narrow the range of pre-shock velocities.

BIBLIOGRAPHY

[dHP+10] T. de Graauw, F. P. Helmich, T. G. Phillips, J. Stutzki, E. Caux, et al., *The Herschel-Heterodyne Instrument for the Far-Infrared (HIFI)*, A&A **518** (2010), L6.

[Gar10] M. A. Garrett, *Radio Astronomy, Lecture 2a,2b (of 14): Radio Telescopes: Antennas, Paraboloids, Performance*, unpublished, www.astron.nl/ mag/dokuwiki/lib/exe/fetch.php? media=radio_astronomy_lec_2_ma_garrett.pdf, 2010.

[GCH09] J. R. Goicoechea, M. Compiègne, and E. Habart, *Far-Infrared Detection of Neutral Atomic Oxygen Toward the Horsehead Nebula*, The Astrophysical Journal Letters **699** (2009), no. 2, L165.

[GLB+11] P. F. Goldsmith, R. Liseau, T. A. Bell, J. H. Black, et al., *Herschel Measurements of Molecular Oxygen in Orion*, ApJ **737** (2011), 96.

[GMB+00] P. F. Goldsmith, G. J. Melnick, E. A. Bergin, J. E. Howe, et al., *O_2 in Interstellar Molecular Clouds*, ApJ **539** (2000), L123–L127.

[HKBM09] D. Hollenbach, M.J. Kaufman, E.A. Bergin, and G.J. Melnick, *Water, O_2, and Ice in Molecular Clouds*, ApJ **690** (2009), 1497.

[HR82] D. G. Hummer and G. B. Rybicki, *A Unified Treatment of Escape Probabilities in Static and Moving Media. I - Plane Geometry*, ApJ **254** (1982), 767–779.

[KN96a] M. J. Kaufman and D. A. Neufeld, *Far-Infrared Water Emission from Magnetohydrodynamic Shock Waves*, ApJ **456** (1996), 611–630.

[KN96b] ———, *Water Maser Emission from Magnetohydrodynamic Shock Waves*, ApJ **456** (1996), 250.

[Liq10] F. Lique, *Temperature Dependence of the Fine-Structure Resolved Rate Coefficients for Collisions of O ($X\Sigma$) with He*, J. Chem. Phys. **132** (2010), 044311.

[LJT06] R. Liseau, K. Justtanont, and A. G. G. M. Tielens, *Outflows from Young Objects Observed with the ISO-LWS*, A&A **446** (2006), no. 2, 561–567.

[MSA+00] G. J. Melnick, J. R. Stauffer, M. L. N. Ashby, E. A. Bergin, G. Chin, N. R. Erickson, et al., *The Submillimeter Wave Astronomy Satellite: Science Objectives and Instrument Description*, ApJ **539** (2000), L77–L85.

[PPM+99] L. Pagani, POM 2, P. Maréchal, B. Langer, et al., *O_2 Search in the Milky Way : New Upper Limits from Ground (POM 2) and Balloon-Borne (PIROG 8) Experiments*, The Physics and Chemistry of the Interstellar Medium (V. Ossenkopf, J. Stutzki, & G. Winnewisser, ed.), August 1999, p. 359.

[PRP+10] Pilbratt, G. L., Riedinger, J. R., Passvogel, T., Crone, G., Doyle, D., Gageur, U., Heras, A. M., Jewell, C., Metcalfe, L., Ott, S., and Schmidt, M., *Herschel Space Observatory*, A&A **518** (2010), L1.

[SvvB05] F. L. Schöier, F. F. S. van der Tak, E. F. van Dishoeck, and J. H. Black, *An Atomic and Molecular Database for Analysis of Submillimetre Line Observations*, A&A **432** (2005), 369–379.

[Ten05] Jonathon Tennyson, *Astronomical Spectroscopy*, Imperial College Press, London, 2005.

[TH85] A. G. G. M. Tielens and D. Hollenbach, *Photodissociation Regions. I - Basic Model. II - A Model for the Orion Photodissociation Region*, ApJ **291** (1985), 722–754.

[Tie05] A. G. G. M. Tielens, *The Physics and Chemistry of the Interstellar Medium*, 1st paperback edition, 2010 ed., Cambridge University Press, 2005.